國　立　交　通　大　學
光　電　系　統　研　究　所

碩 士 論 文

利用埋入式次波長奈米結構提升非晶矽太陽能電池光捕捉效率

Enhanced Light Trapping in Thin Film a-Si Solar Cell by Embedded Front Pre-patterned Substrate

研究生：韓皓惟

指導教授：郭浩中教授

林建中教授

中華民國一百年七月

利用埋入式次波長奈米結構提升非晶矽太陽能電池光捕捉效率

Enhanced Light Trapping in Thin Film a-Si Solar Cell by Embedded Front Pre-patterned Substrate

研究生：韓皓惟　　Student：Hao-Wei Han

指導教授：郭浩中 教授　　Advisor：Hao-Chung Kao

林建中 教授　　Chien-Chung Lin

國 立 交 通 大 學

光 電 系 統 研 究 所

碩 士 論 文

A Thesis

Submitted to Institute of Photonic System

College of Photonics

National Chiao Tung University

in Partial Fulfillment of the Requirements

for the Degree of

Master

In

Photonic System

July 2011

Tainan, Taiwan, Republic of China

中華民國一百年七月

利用埋入式次波長奈米結構提升非晶矽太陽能電池光捕捉效率

研究生：韓皓惟　　指導教授：郭浩中、林建中

國立交通大學光電系統所

論文摘要

隨著矽原料的短缺及降低成本的的考量，矽薄膜太陽能電池日益受到重視，但也由於材料厚度的減少，吸收效率隨之下降，其中更以紅外波段影響甚大，因此如何有效的增加光在矽材料中的光學路徑，實為矽薄膜太陽能電池之重要課題。

傳統上的光捕捉結構主要是製做於元件的背面，只能藉由繞射或散射增加通過主動層而還沒有被完全吸收的光線之光學路徑長，但這樣的光捕捉結構往往就沒有抗反射效果。在本論文中，我們試圖利用一個結構應用於非晶矽太陽能電池之上，能有效增加非晶矽太陽能電池元件的光電流以及光電轉換效率。我們採用旋塗法搭配奈微米球微影術這種大面積、便宜又快速的方法，加上非等向性蝕刻達到控制次波長形貌的效果，在事先沈積在玻璃透明基板上的氮化矽薄膜蝕刻出蛋型次波長奈米結構，再於其上利用真空濺鍍系統、高密度電漿化學氣相沈積系統、以及電子槍金屬蒸鍍系統依序沈積透明導電層、非晶矽主動層、和金屬背反射層，而製作出位於入光面且埋入非晶矽主動層的奈米結構，來同時達到抗反射和光捕捉的效果。

我們可經由積分球吸收頻譜的量測而明確的看見結構所帶來的優異的抗反射和光捕捉效果，甚至在光線大角度入射元件時，奈米結構依然可以提供更勝於傳統多層膜抗反射層的表現。短路電流密度可有效的大幅增加，進而將元件光電轉換效率由原本的5.36%提升至 8.38%。最後我們還利用三維的嚴格耦合波分析(rigorous coupled wave analysis)模擬軟體進行結構的最佳化，進一步預測在製程可行的範圍內，不同的結構寬度及高度對元件吸收及產生之光電流密度的模擬，可由此得知往後實際實驗的方向，並減少製程上不必要的測試與時間。

Enhanced Light Trapping in Thin Film a-Si Solar Cell by Embedded Front Pre-patterned Substrate

Student: Hao-Wei Han Advisors: Prof. H. C. Kuo, Prof. C. C. Lin

Institute of Photonic System, National Chiao Tung University

ABSTRACT

Light trapping in amorphous silicon thin film solar cells has been an intensive study owing to the low absorption coefficient in near-infrared. We demonstrate a frontal pre-patterned substrate (PPS) on amorphous silicon solar cells, utilizing scalable colloidal lithography, to serve both functions of anti-reflection at short wavelength and light trapping effect at long wavelength. We measured the absorption spectrum by an integrating sphere at normal incidence and the external quantum efficiency (EQE) of three type structures. The power conversion efficiency of the pre-patterned cell is measured 8.38%, which shows 56.34% and 8.83% enhancement compared to the reference cell with a flat substrate and the commercialized Asahi U-type substrate, respectively. The increased efficiency is mainly resulted from the enhanced short-circuit current density (from 12.89 mA/cm^2 to 19.77 mA/cm^2).

Moreover, the angle-resolved absorption spectroscopy shows superior optical coupling to the absorber layer at large angles of incidence (AOIs), which guarantees sufficient light harvesting for the entire day. We also present a design optimization of frontal pre-patterned substrate with broadband antireflective subwavelength structures based on the theoretical calculation using a three-dimensional rigorous coupled wave analysis (RCWA) method. The best structure on our pre-patterned substrate is 500 nm bottom width and 400~450 nm height of SiNx nipple pattern.

Acknowledgements

時間過得真快，碩士班的兩年匆匆過去，回想這兩年來的點點滴滴彷彿一切都在昨天，好像大家才很生澀地踏進這生活兩年的實驗室怎麼突然又要跟大家分別。在這短暫的兩年中，參予了實驗室許多大大小小的活動，一路上也受到很多人的幫助，今天才能對實驗室有一點貢獻完成這一篇的碩士論文。很高興兩年前的選擇是正確的，有幸加入交大光電所的半導體雷射實驗室，首先當然要感謝我的兩位指導教授-郭浩中老師以及林建中老師，在實驗上盡其所能地給予協助以及提供豐富的研究資源，在郭老師的督促與指導下讓我在待人處事與個人發展上都受益良多，而和藹可親且學識淵博的林老師在我需要協助時所給予的幫助讓我難以忘懷。並且感謝口試委員余沛慈老師以及賴芳儀老師對我論文的建議與指教，在口試時的寶貴建議讓我的論文能夠更加嚴謹及完整。

感謝我們太陽能組的兩位領導學長-蔡閔安學長以及曾斌誠(Micheal)學長，在這兩年的碩士班期間一路伴著我成長，實驗上的困難或是模擬的問題總是不厭其煩的教導我。永遠充滿活力且活蹦亂跳的閔安學長在我遇到困難時總能給我一個樂觀的方向去嘗試，能想出許多千奇百怪的方法去解決，但做實驗時卻又能拿出身為物理博士的嚴謹與態度，在問題處理以及領導能力上讓我著實獲益良多。理論及語言能力超強的 Micheal 學長在我對模擬有問題的任何時候去找他，他都能鉅細靡遺的告訴我所有過程的來龍去脈，喜歡思考的個性讓他在實驗上能夠提出許多獨到的見解，是我在實驗上學習的楷模。另外還要感謝信助學長以及珣彣學姊，有著一顆真誠的心的信助不時給我許多鼓勵與加油，而愛聊天的珣彣學姊總是在做實驗時跟我分享很多的人生經驗。最後是認識還不到一年有著深厚的物理背景的祐廣，希望將來我們能一起繼續努力。

再來感謝實驗室的夥伴們：羿蓁、瑋婷、Jolin、大寶、幼齒、阿 PO、家齊、祐國、小杜、峰瑜、冠霖、KaKa、大頭、SGG、Just、季瑾。謝謝你們大家豐富了我的碩班生活，給予了我一段從來沒有的多采多姿的求學經歷。我永遠都記得當初我們剛到實驗室來，大家排排坐在工五 250 公用座位的情形，我們的友情就從那時開始萌芽。無法計數

的美食團，一群人騎著摩托車浩浩蕩蕩立志要吃遍全新竹，發掘新竹美食沙漠的綠洲的夢想。還有趁著實驗閒暇之餘，上山下海走透透一次又一次的出遊，每個景點現在想來都歷歷在目。人小鬼大、活潑熱情的羿蓁有妳在的地方就會有活動，無論是熬夜打牌還是促膝長談都少不了妳，總是能沒有距離和我們玩成一團，我碩班兩年的綽號也是因妳而起，叫久了也是蠻習慣蠻親切的。還有天真善良、文靜可愛的瑋婷，喜歡聽妳分享那些天馬行空的想法與夢境，和妳相處總不時出現意外卻很可愛的有趣場面，謝謝妳總是對我非常的信任，看到妳在水中緩慢的前進讓我非常的有成就感。再來是我的好搭擋Jolin，兩年來多謝你在製程上的幫助，很多的時候我們彼此交換意見，在 meeting 上、在飯局中、或在夜晚的 H 棚停車場，雖然也會有意見不合的時候，但總是在這樣的摩擦中才能讓我們的默契越來越好，很高興能和你成為夥伴，希望在接下去的博士班生涯我們能繼續互相幫助與合作。還有大寶和幼齒兩位哥兒們，雖然平常鬥鬥嘴開開玩笑，但在需要幫助時總是兩肋插刀讓我印象深刻，且擁有高超的攝影技術為我們兩年的點點滴滴做了紀錄，真是辛苦你們了。感謝阿 PO 成為我們出團的基本角色之一，雖然常常不知道你到底有沒有搞清楚狀況，但你總是會參加到底。謝謝家齊不厭其煩的為我們大家解釋紙牌遊戲的遊戲規則，年紀最輕卻是頭腦最靈活的一員。還有好學生祐國，和你討論課業上的問題總是很有收穫，英文能力超強也是我的楷模之一。感謝阿莎力且喜歡交朋友的小杜，出遊時有你在就永遠有歡笑。感謝帥氣的峰瑜，你那爽朗的笑聲有將歡笑散播給大家的傳染力，在親切的笑容背後卻有著成熟穩重的個性。感謝平日不多話的冠霖，有著一顆精打細算的頭腦，股票哪天有明牌記得偷偷洩漏給我知道。感謝擁有強烈卡式風格的 KaKa，慢了好幾拍的反應常常讓我們笑到肚子痛，超隨和的個性讓我們對妳開玩笑也從來不生氣。接著是 NDL 一哥大頭，超挺朋友的你在我需要實驗上的幫忙時總是義不容辭。再來是新竹美食通 SGG，對每一間餐廳瞭若指掌讓我這個新竹人也訝異。還有盧老師愛將 Just，在接下來的博士班生涯裡希望繼續互相協助。最後是不常出現在實驗室的季瑾，碰面時總會停下腳步跟我聊上兩句，互相交換一下近日的生活。另外還要特別感謝施懷翔和曹廷耀兩位學弟，在這一年來在實驗與模擬上的幫助，有了你們替我分擔了不少負擔，也希望你們在接下來的學業研究一切順利。

最後要感謝我最親愛的家人，你們的默默付出讓我才能無後顧之憂地完成碩士學業，你們對我的關心與體貼是我碰到困難時最大的精神支柱，有你們陪伴在我身旁我就是全世界最幸福最幸運的人，謝謝你們!

Content

摘要.....i

Abstract.....ii
Acknowledgements.....iii
Content.....vi
List of Tables.....viii
List of Figures.....ix

Ⅰ. Introduction.....1

1.1 The Development of Solar Cells.....2
1.2 About Thin Film Solar Cells.....5
1.3 Motivation.....8

Ⅱ. Basic Theories of Solar Cell.....10

2.1 Basic principle of solar cell.....10
2.2 The Equivalent Circuit Analysis of The Solar Cell.....12

Ⅲ. Experimental and Measuring Instruments.....18

3.1 Plasma-enhanced chemical vapor deposition (PECVD).....18
3.2 Scanning electron microscope (SEM).....19
3.3 Transmission electron microscopy (TEM).....20
3.4 Integrating sphere reflectance measurement.....21
3.5 Power conversion efficiency measurement.....24
3.6 External quantum efficiency measurement.....25

Ⅳ. Light Management.....27

4.1 Minimizing Reflection.....27

4.1.1 Optical properties of semiconductor.....27

4.1.2 Anti-reflection coatings.....29

4.2 Light confinement.....33

Ⅴ. RCWA (Rigorous Coupled-Wave Analysis) Method.....35

Ⅵ. Application of embedded sub-wavelength substrate on amorphous silicon thin film solar cell.....38

6.1 Fabrication processes.....40

6.2 Experimental results and discussions.....45

6.2.1 Integrating sphere reflectance measurement.....46

6.2.2 External quantum efficiency measurement.....47

6.2.3 Power conversion efficiency measurement.....49

6.3 Angular absorption.....51

6.4 Simulation.....51

Ⅶ. Conclusion.....54

Reference.....55

List of Tables

Table 4.1 Refractive indices of selected semiconductors and AR coat materials.....28

Table 6.1 The detail electrical information of J-V measurements.....50

List of Figures

Figure 1.1 The energy usage trends in 2000 to 2100. The primary energy is the currently used energy by humans including coals and oils. But in the future, as the reduction of the stock of primary energy is bound to be replaced by green energy. The solar energy used in electricity generation in 2100 will be on the leading energy demand..... 2

Figure 1.2 This is the classification of various materials and the efficiency of solar cells under the standard solar simulator irradiation measurement.....4

Figure 1.3 (a) Absorption coefficients of a number of different photovoltaic materials. (A derivative of the organic semiconductor polyphenylene vinylene (MDMO-PPV) is included for comparison.); (b) Maximum photon current available from each material under AM1.5 illumination, as a function of film thickness, assuming perfect collection of all photogenerated charges. The saturation photocurrent is a function of band gap. The maximum photocurrent supplied by the Am1.5 spectrum is around 49 $mAcm^{-2}$.....7

Figure 2.1 Structure of the basic components of solar cells.....10

Figure 2.2 The diagram of photovoltaic effect.....11

Figure 2.3 The electron-hole pairs generated in the depletion layer and separated by the electric-field built-in voltage (V_{bi}).....11

Figure 2.4 The diagram of solar cell equivalent circuit.....12

Figure 2.5 The I-V characteristics with and without illumination.....13

Figure 2.6 Effect of increasing series and reducing parallel resistances. In each case the outer curve has $R_s = 0$ and $R_{sh} = \infty$. In each case the effect of the resistances is to reduce the area of the maximum power rectangle compared to $J_{sc} \times V_{oc}$.....17

Figure 3.1 (a) Schematic diagram of conventional reflectivity measurements. (b) Schematic diagram of Integrating sphere reflectance measurements.....22

Figure 3.2 Schematic diagram of integrating sphere in our laboratory.....23

Figure 3.3 Schematic diagram of energy conversion efficiency measurement, including a solar simulator, a Keithley 2400 digital power meter for the measurement of electrical characteristics, and a computer with Labview program to process the measurement data.....24

Figure 3.4 The erection diagram of grating-based mono-chrometer for the quantum efficiency.....25

Figure 4.1 Single layer anti-reflection coating. When the thickness of the dielectric layer is equal to one quarter wavelength, the incident and reflected waves interfere destructively to cancel out the reflected ray at the outer surface.....29

Figure 4.2 Calculated reflectivity of single layer AR coat as function of wavelength at different angles of incidence $\theta = 0^\circ, 30^\circ, 60^\circ$. Notice how the minimum of reflectivity lifts and shifts to shorter wavelengths at wider angles of incidence. Calculated for a 100 nm layer of refractive index $n_1 = \sqrt{3.3}$ on top of a semiconductor of refractive index $n_s = 3.3$.....31

Figure 4-3 Calculated reflectivity of double layer AR coat, optimized for 700nm. The reflectivity of a single layer is presented for comparison.....32

Figure 4.4 Light trapping structure with a tilted rear surface, illustrating a 'double bounce' light path.....34

Figure 5.1 The schematic picture of a simple case in the RCWA method. The light is launched from the superstrate region. The analyzed structure is a grating. In the algorithm of RCWA method, all the periodic structures will be split up many such simple grating forms.....35

Figure 6.1 In this study, the process of pre-prepared samples. (a) The silicon nitride (SiN_x) of 500 nm was deposited on a glass substrate by using plasma-enhanced chemical vapor deposition (PECVD). (b) The polystyrene (PS) nanospheres was spun on the surface of the SiN_x layer, forming a close-packed monolayer mask, and then shrink the size of the PS spheres.....40

Figure 6.2 The top view SEM images of the closely packed polystyrene nanospheres on the SiN_x layer.....41

Figure 6.3 The device fabrication process of front pre-pattern substrate a-Si solar cell.....42

Figure 6.4 Scanning electron microscopic (SEM) images of the fabricated SiNx nipple arrays: (a) a 45-degree tilted top view and (b) a cross-sectional view.....43

Figure 6.5 The cross-sectional TEM image of a fabricated solar cell on the pre-patterned substrate.....43

Figure 6.6 SEM image of the Asahi U-type sample.....44

Figure 6.7 AFM image of the Asahi U-type sample.....44

Figure 6.8 Schematic diagram of the sub-wavelength structure for antireflective by gradient refractive index. When the nano-structures is less than the wavelength of incident light, this anti-reflective nano-structure layer can use spatial gradient structure to achieve the effect of graded refractive index. The structure close to the end of air is a higher air ratio and a low refractive index, but the structure close to the end of structure is a lower air ratio and a high refractive index.....45

Figure 6.9 The spectrum of cell absorption at normal incident.....46

Figure 6.10 The external quantum efficiency (EQE) of the cell for three type substrates.....47

Figure 6.11 The improvement factors of the EQE (*ΔEQE*) for EBN and Asahi U, (a) between 400 nm and 600 nm, and (b) between 600 nm and 800 nm.....48

Figure 6.12 The internal quantum efficiency (IQE) of the cell for three type substrates.....49

Figure 6.13 J-V measurements of the flat reference, PPS, and Asahi U cells.....50

Figure 6.14 The angle-resolved absorption spectroscopy for the cell with the (a) flat substrate and (b) PSS substrate.....51

Figure 6.15 The cross section of simulation model structure and the modulation parameters.....52

Figure 6.16 The calculated short-circuit current density enhancement compared to the reference flat cell as a function of the bottom width (W) and height (H) of SiNx nipple pattern.....53

Ⅰ. Introduction

Since the development of the global environment has passed hundreds of thousands of years, as technology advances and the development of capacity and population growth, growing demand for expansion of the Earth's resources. IEA (International Energy Agency, IEA) mentioned in 2007 and 2030 global energy demand will grow by 1.5% at World Energy Outlook 2009, while after 2030 the world's electricity demand is expected to increase the rate of 2.5% per year [1]. Coal is still the main fuel of power generation industry. However, the one of main cause is derived from the carbon dioxide caused by continued growth in global carbon dioxide emission. This will certainly lead to a long large-scale climate change. It will give the irreparable harm to the earth. So, how to effectively reduce carbon dioxide emission is the common face of the issue.

In this regard, an energy revolution can be expected, and the rise of green energy will play a big lead of the energy revolution. The green energy is a reusable and less polluting energy sources, such as wind, solar, geothermal, tidal, etc. Solar energy has a very large number of sources of supply. Because the sun produces about 1.76 × 105 MW energy per year, of which 600 MW irradiation on the surface of the earth are available. Its energy is 100,000 times than the global average power. With technological advances, our solar energy use efficiency is also increased. It is expected for a large proportion in the next available energy sources account. From Figure 1.1, we can see the future of solar energy usage is expected to continue to rise.

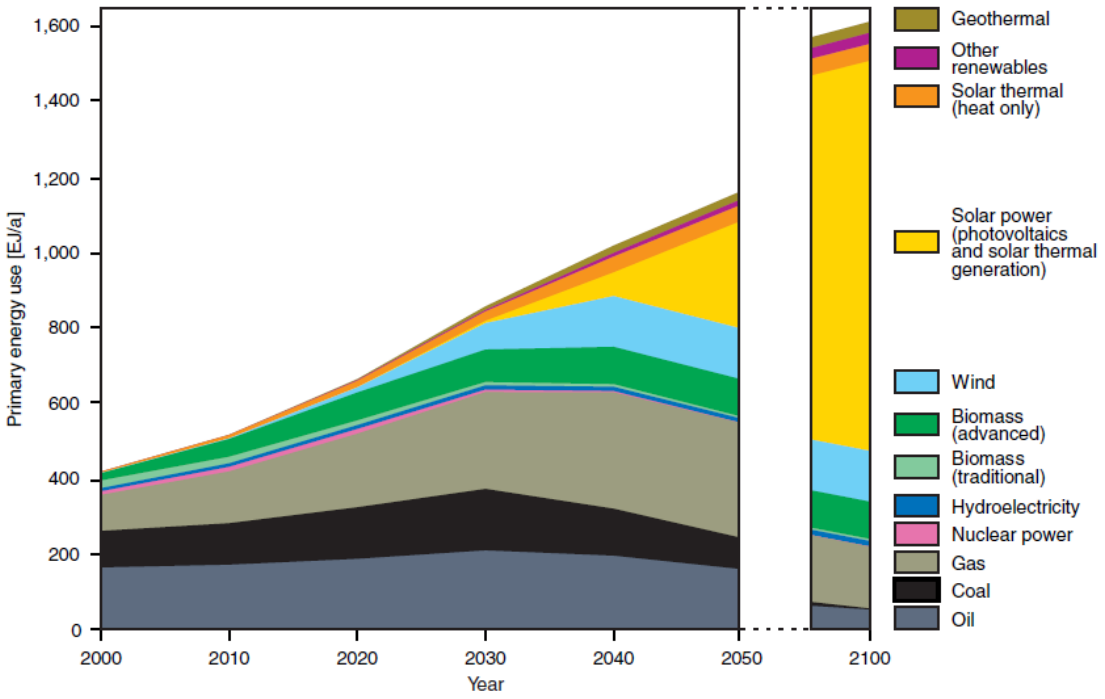

Figure 1.1 The energy usage trends in 2000 to 2100. The primary energy is the currently used energy by humans including coals and oils. But in the future, as the reduction of the stock of primary energy is bound to be replaced by green energy. The solar energy used in electricity generation in 2100 will be on the leading energy demand.

1.1 The Development of Solar Cells

The development of the solar cell stems from the work of the French physicist Antoine-César Becquerel in 1839. Becquerel discovered the photovoltaic effect while experimenting with a solid electrode in an electrolyte solution; he observed that voltage developed when light fell upon the electrode. About 50 years later, Charles Fritts constructed the first true solar cells using junctions formed by coating the semiconductor selenium with an ultrathin, nearly transparent layer of gold. Fritts's devices were very inefficient, transforming less than 1 percent of the absorbed light into electrical energy.

By 1927 another metal-semiconductor-junction solar cell, in this case made of copper and the semiconductor copper oxide, had been demonstrated. By the 1930s both the selenium cell and the copper oxide cell were being employed in light-sensitive devices, such as photometers, for use in photography. These early solar cells, however, still had energy-conversion efficiencies of less than 1 percent. This impasse was finally overcome with the development of the silicon solar cell by Russell Ohl in 1941. In 1954, three other American researchers, G.L. Pearson, Daryl Chapin, and Calvin Fuller, demonstrated a silicon solar cell capable of a 6-percent energy-conversion efficiency when used in direct sunlight. By the late 1980s silicon cells, as well as those made of gallium arsenide, with efficiencies of more than 20 percent had been fabricated. In 1989 a concentrator solar cell, a type of device in which sunlight is concentrated onto the cell surface by means of lenses, achieved an efficiency of 37 percent due to the increased intensity of the collected energy. In general, solar cells of widely varying efficiencies and cost are now available [2]. After the oil crisis, the most of the world's countries alerted the important of new alternative energy development. The sun is just inexhaustible natural energy, neither energy depletion concerns, but also avoids the problem of energy monopoly. Therefore, countries actively developed the application of solar energy technology, expected by increasing the use of solar energy to reduce dependence on primary energy. The solar cell conversion efficiency research began to flourish. Today's market-oriented solar cells can be focus on the conversion efficiency of about range of 10% to 36% [3], while the theoretical maximum efficiency can reach 86% [4]. It can be seen that in the photoelectric conversion efficiency we have a lot of space to develop these technologies which will be a great help to solve the international community energy crisis in the future.

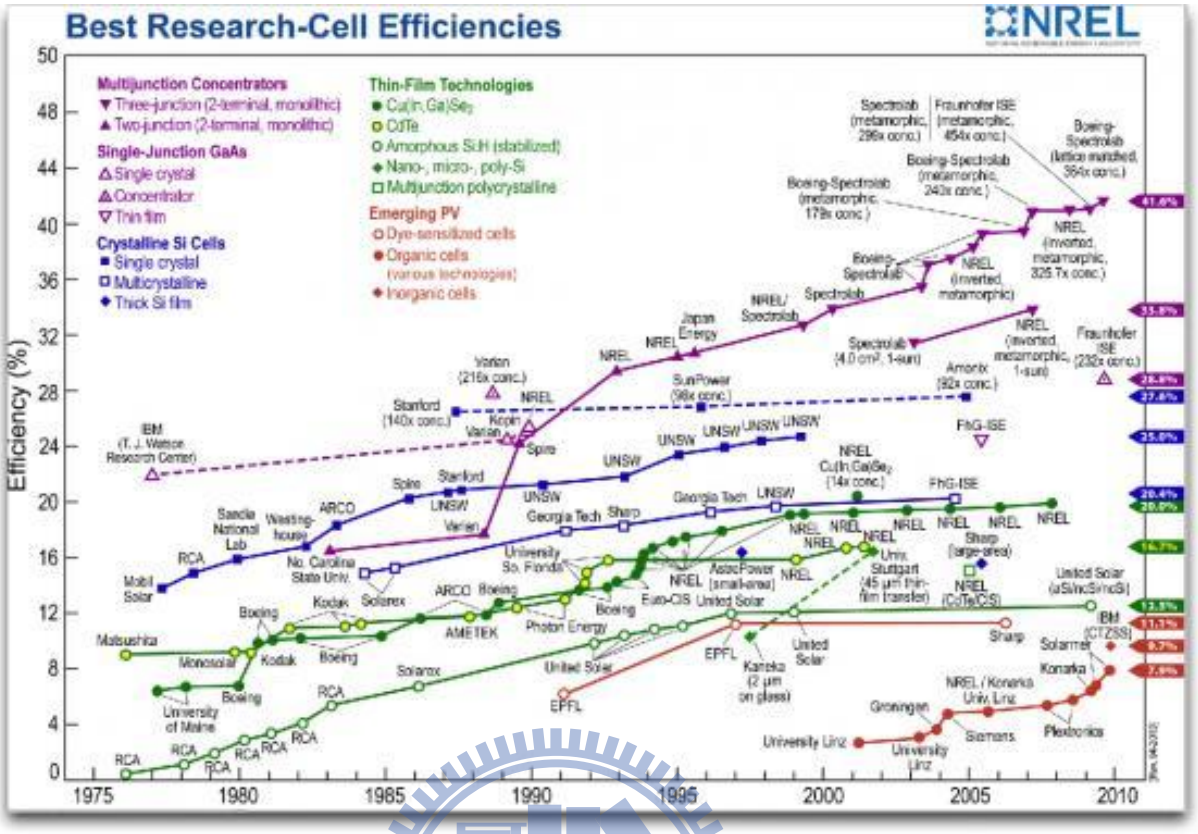

Figure 1.2 This is the classification of various materials and the efficiency of solar cells under the standard solar simulator irradiation measurement.

According to different materials and fabrication process methods can be divided into different types of solar cells. Material visible on the market today include: silicon materials (single crystal silicon, polycrystalline silicon, amorphous silicon), III-V semiconductor (GaAs) materials, II-VI semiconductor (CdS / CdTe) materials and organic materials (TiO2) and so on. Figure 1.2 is the current solar cell material types and their efficiency comparison chart. The GaAs solar cells is highest for the current efficiency, its efficiency can be as high as 30% or more, but it is expensive and containing highly toxic. In the early, it is used on the defense industry and space satellites, most recently the III-V semiconductor (GaAs) materials has been used to people's livelihood for the high-efficiency concentrator solar power system. However, the organic solar cells are used in the commercial market yet, but it is really the direction of study at domestic and international. Although the photoelectric conversion

efficiency of organic solar cells is currently low, but the process is simple, low cost, and has advantages of transmittance, large area manufacturing and can combine with the flexible substrate. CIGS solar cell with low cost, long life and high efficiency potential is a lot of companies to invest in emerging industries, but there is no standardization of products and technical specifications. The CIGS solar cells used the indium material to fabricate. According to scholar's statistic, the indium material left about 10,000 tons in the whole world. The next problem that CIGS solar cell has to face is lack of material in the future. Silicon solar cell technology is currently the most mature and widely applied. There are three types of silicon solar cells, including single-crystal silicon, polycrystalline silicon, and amorphous silicon solar cells. And single-crystal silicon and polycrystalline silicon solar cells are technically more mature and can be mass production.

1.2 About Thin Film Solar Cells

We have seen that , provided that minority carrier diffusion lengths exceed typical absorption depths, p-n junctions make efficient photoconverters with a high collection efficiency, where recombination at the surfaces is the dominant loss process. However, single crystals are expensive to produce and so there is a great deal of interest in finding photovoltaic materials of less demanding material quality which can be grown more cheaply. A number of materials have been identified of which the best developed at present are amorphous silicon (a-Si), polycrystalline cadmium telluride (CdTe), poly-crystalline copper indium diselenide ($CuInSe_2$) and microcrystalline thin film silicon (μ -Si). These 'thin film' materials are usually produced by physical or chemical deposition techniques which can be applied to large areas and fast throughput.

Polycrystalline and amorphous semiconductors contain intrinsic defects which increase the density of traps and recombination centers. For solar cells, this has the consequence that:

- Diffusion lengths are shorter, so the material needs to be a strong optical absorber. Alternatively, multiple junctions must be used to make the device optically thick. In the case of very short diffusion lengths, it may be necessary to use extended built-in electric field to aid carrier collection. This is the case in amorphous silicon, where p-i-n structures are preferred.
- Losses in the layers close to the front surface are greater, so it is advantageous to replace the emitter with a wider band gap window material.
- The presence of defect states in the band gap can make the materials difficult to dope, and limit the built-in bias available from a junction through Fermi level pinning.
- The presence of grain boundaries and other intrinsic defects increases the resistivity of the film particularly at low doping densities, and males the conductivity dependent on the carrier density, so influencing the electrical characteristics of devices.
- The presence of defects similarly means that minority carrier lifetime and diffusion constant are carrier density dependent.

Good thin film materials should be low cost, non-toxic, robust and stable [5]. They should absorb light more strongly than silicon. Higher absorption reduces the cell thickness and so relaxes the requirement for long minority-carrier diffusion lengths, allowing less pure polycrystalline or amorphous materials to be used. Figure 1.3 compares the absorption coefficients for several photovoltaic materials and the maximum photo current which can be generated in a thin film as a function of its thickness. Notice how weakly crystalline silicon absorbs, in comparison with the other materials. Suitable materials should transport charge efficiently, and should be readily doped. Materials are particularly attractive if they can be

deposited in such a way that arrays of interconnected cells can be produced at once (Figure. 1.3). This greatly reduces the module cost.

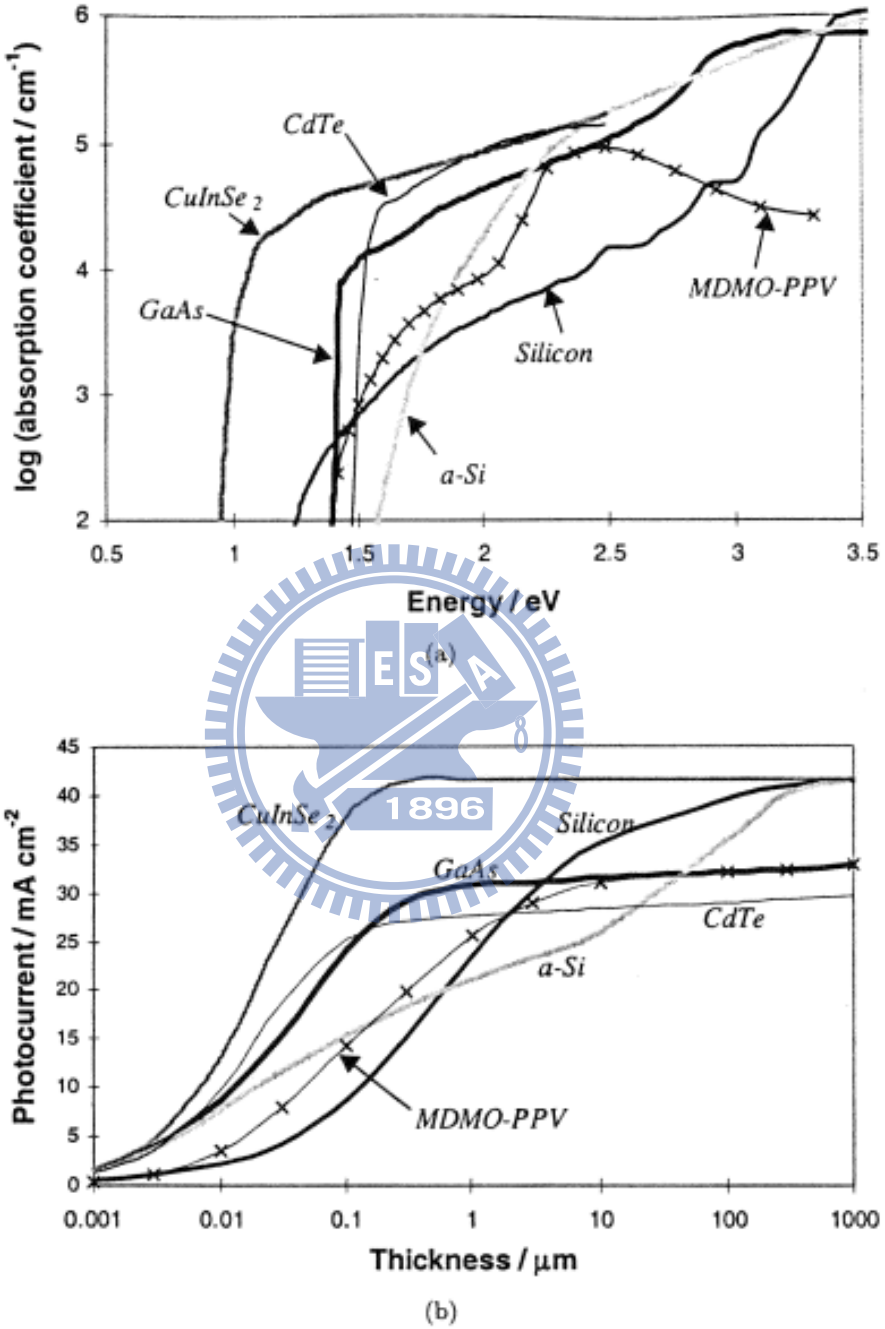

Figure 1.3 (a) Absorption coefficients of a number of different photovoltaic materials. (A derivative of the organic semiconductor polyphenylene vinylene (MDMO-PPV) is included for comparison.); (b) Maximum photon current available from each material under AM1.5 illumination, as a function of film thickness, assuming perfect collection of all photogenerated charges. The saturation photocurrent is a function of band gap. The maximum photocurrent supplied by the Am1.5 spectrum is around 49 mAcm^{-2}. [6]

Of the elemental semiconductors, only silicon has a suitable band gap for photovoltaic energy conversion. Compound semiconductors greatly extend the range of available materials and of these a number of Ⅱ-Ⅵ binary compounds and Ⅰ-Ⅲ-Ⅵ ternary compounds have been used for thin film photovoltaics. Many of these are direct band gap semiconductors with high optical absorption relative to silicon. The Ⅰ-Ⅲ-Ⅵ compounds (or chalcogenides) are analogous to Ⅱ-Ⅵ's where the group Ⅱ element has been replaced by a group Ⅰ and a group Ⅲ species. At present the leading compound semiconductors for thin film photovoltaics are the Ⅱ-Ⅵ semiconductor, CdTe, and the chalcogenide alloys, $CuInGaSe_2$ and $CuInSe_2$. Other new materials are continually being investigated, including other Ⅱ-Ⅵ and Ⅰ-Ⅲ-Ⅵ compounds, amorphous carbon and nanocrystalline silicon [6].

1.3 Motivation

To meet the solar cells trend demands "thin film, high efficiency and low-cost", amorphous silicon solar cell is an excellent choice. Amorphous material has the following advantages: no restrictions on the supply of materials, production capital is low, with the prospect of lower production costs, and for the environment and human health effects at a lower overall total benefits, with the exception of its conversion efficiency is still less than the current single-crystal silicon and III-V material solar cells. To overcome the lack of efficiency and cheaper production costs to make the most direct way that is to improve the amorphous silicon solarcells efficiency of power generation unit. Antireflection layer (AR coating) is traditionally widely used for various auxiliary structure of solar cells, which allows more usable light into the active layer of solar cell to be absorbed. In addition, the amorphous silicon thin-film solar cells are one type of solar cell, the absorption layer thickness of such cells is often not long enough, so the light trapping structure is become more important. By

the light trapping structure we are able to capture light into the active layer of solar cell to stay longer, and use this way to compensate for the problem of inadequate absorption layer thickness. In my thesis, we start from these two effects. We use nanosphere lithography technique to make nano-scale sbuwavelength structure, and we achieve these two effects, antireflection coating and light trapping, in the same structure simultaneously. As the perception, Sub-wavelength structures with wide spectrum anti-reflective and light capture effect can both applied on the amorphous silicon solar cells, it is expected to produce superior photocurrent and conversion efficiency. In this thesis, we will make out the actual structure, and use the solar cell efficiency measurement system and the frequency response of the external quantum efficiency measurement to make the electrical analysis. At the same time in this thesis, we also use simulation software for rigorous coupled wave analysis (RCWA), and to study the optical characteristic of nano-structure. The Rigorous Coupled-Wave Analysis (RCWA) method calculates the diffraction efficiency and field distribution for a 2D or 3D periodic structure. It helps in the design process of applications such as sub-wavelength structures, photonic band gap crystals, and other grating-assisted devices. We use this simulation method to calculate the diffraction efficiency of each diffraction series, transmittance and other properties, and to simulate the actual experimental results then combine with the experimental to achieve the optimization of process parameters. It is accelerated the amorphous silicon thin film solar cells in research and development speed, but also reduce the development process time and resource consumption.

Ⅱ. Basic Theories of Solar Cell

2.1 Basic principle of solar cell

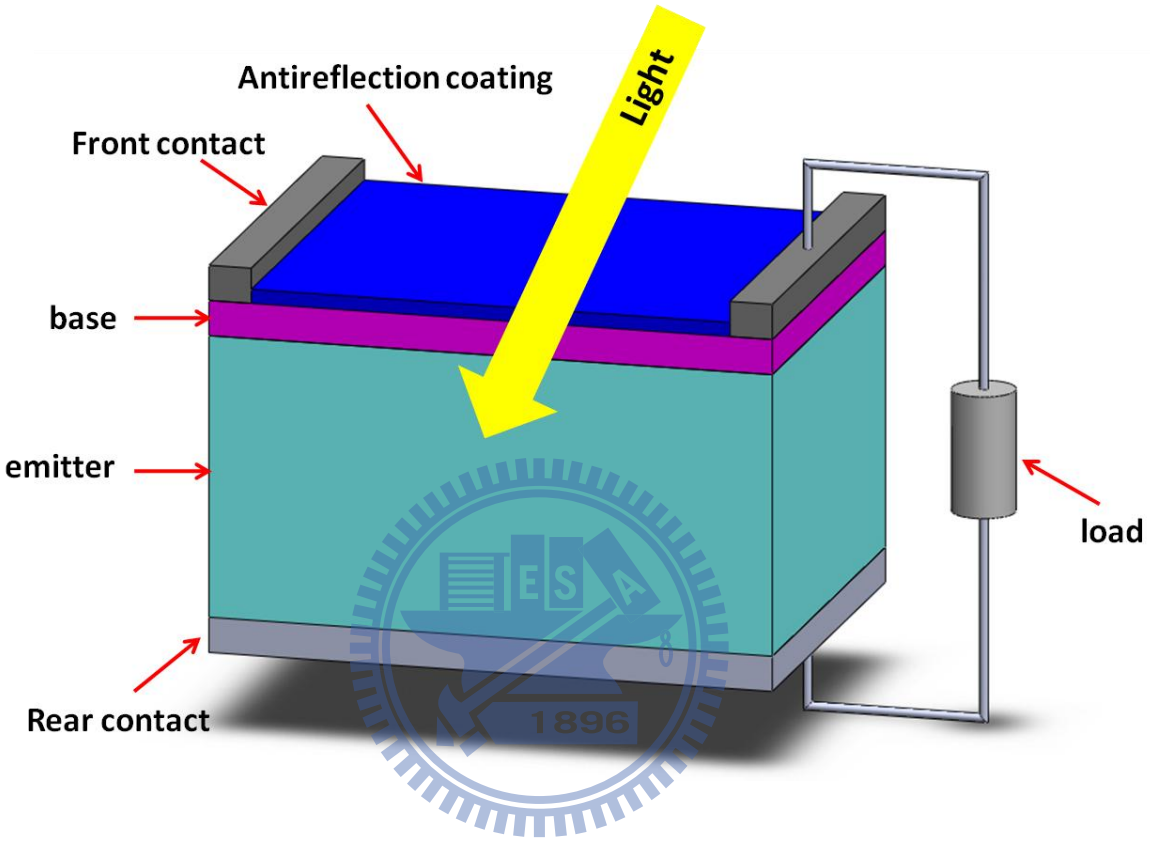

Figure 2.1 Structure of the basic components of solar cells [7][8].

The photovoltaic effect is a phenomenon in which electrons are emitted from matter after the absorption of energy from electromagnetic radiation such as X-rays or visible light. Figure 2.2 shows the diagram of the photovoltaic effect. If the energy of incident light is greater than or equal to energy gap (hv ≧ Eg), electrons could be promoted from ground states to excited states generating electron-hole pairs.

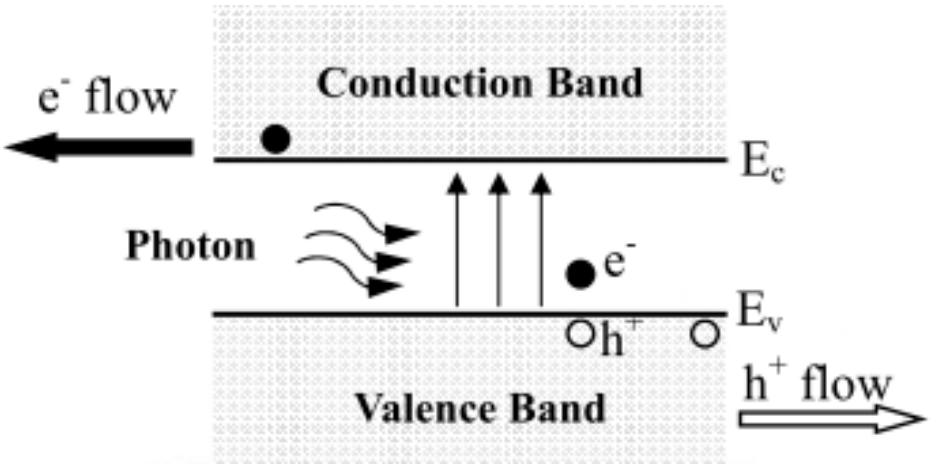

Figure 2.2 The diagram of photovoltaic effect.

The electron-hole pairs generated in the depletion layer are separated by electric-field built-in voltage (V_{bi}) and drift to the n-type and p-type region shown in Figure 2.3 [9]. In the n region and the p region, there is no electric-field (quasi-neutral regions) that the photo-generated electron-hole pairs would not be separated by the electric-field and they would be essentially recombined with the majority carriers. Therefore, the photocurrent of the solar cell device mainly comes from photo-generated carries in the depletion region [10].

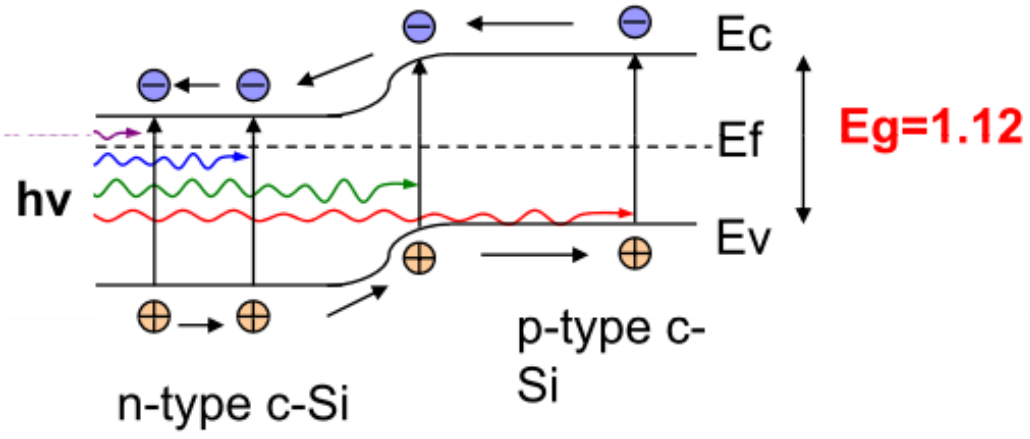

Figure 2.3 The electron-hole pairs generated in the depletion layer and separated by the electric-field built-in voltage (V_{bi}).

2.2 The Equivalent Circuit Analysis of The Solar Cell

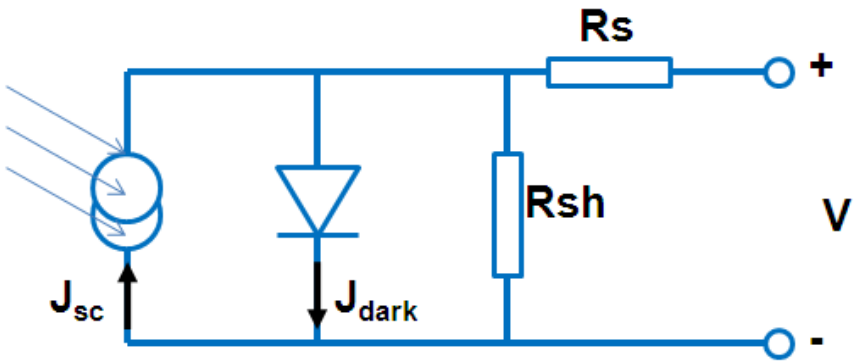

Figure 2.4 The diagram of solar cell equivalent circuit.

Figure 2.4 illustrates the equivalent circuit of solar cell. From this diagram, one could find the photo-generated current (I) as follows [11]:

$$I = I_{sc} - I_0\left\{\exp\left[\frac{q(V+IR_s)}{nkT}\right] - 1\right\} - \frac{V+IR_s}{R_{sh}} \quad (2\text{-}1)$$

where I_{sc} is the short-circuit current (also called light-generated current, I_L), I_0 is the reverse saturation current of the diode, k is the Boltzmann's constant, T is the absolute temperature in degrees Kelvin, n is the ideality factor of diode ($1 < n < 2$, n=1 for the Shockley equation), R_s is the equivalent series resistance and R_{sh} is the equivalent shunt resistance of the solar cell. An idealized solar cell, the series resistance R_s is close to infinity and treats as open in the equivalent circuit. Therefore, the Eq. (2-1) can simplified as:

$$I = I_{sc} - I_0\left[\exp\left(\frac{qV}{nkT}\right) - 1\right] \quad (2\text{-}2)$$

In Figure 2.4, when the intensity of solar radiation is weak, the current of diode is approximately the leakage current ($I_d \approx \frac{V_d}{R_{sh}}$), therefore, R_s can be ignore and R_{sh} effect is important, then Eq. (2-1) can be rewritten as:

$$I = I_{sc} - I_0\left[\exp\left(\frac{qV}{nkT} - 1\right)\right] - \frac{V}{R_{sh}} \quad (2\text{-}3)$$

When the intensity of solar radiation is great, the light-generated current is great and diode is on condition. Therefore, the current of diode is greater than the leakage current ($I_d \gg \frac{V_d}{R_{sh}}$), and the Rsh can be ignore and the Rs effect is important. Then the Eq. (2-1) can be rewritten as:

$$I = I_{sc} - I_0 \left[\exp\left(\frac{qV+IR_s}{nkT}\right) - 1\right] \quad (2\text{-}4)$$

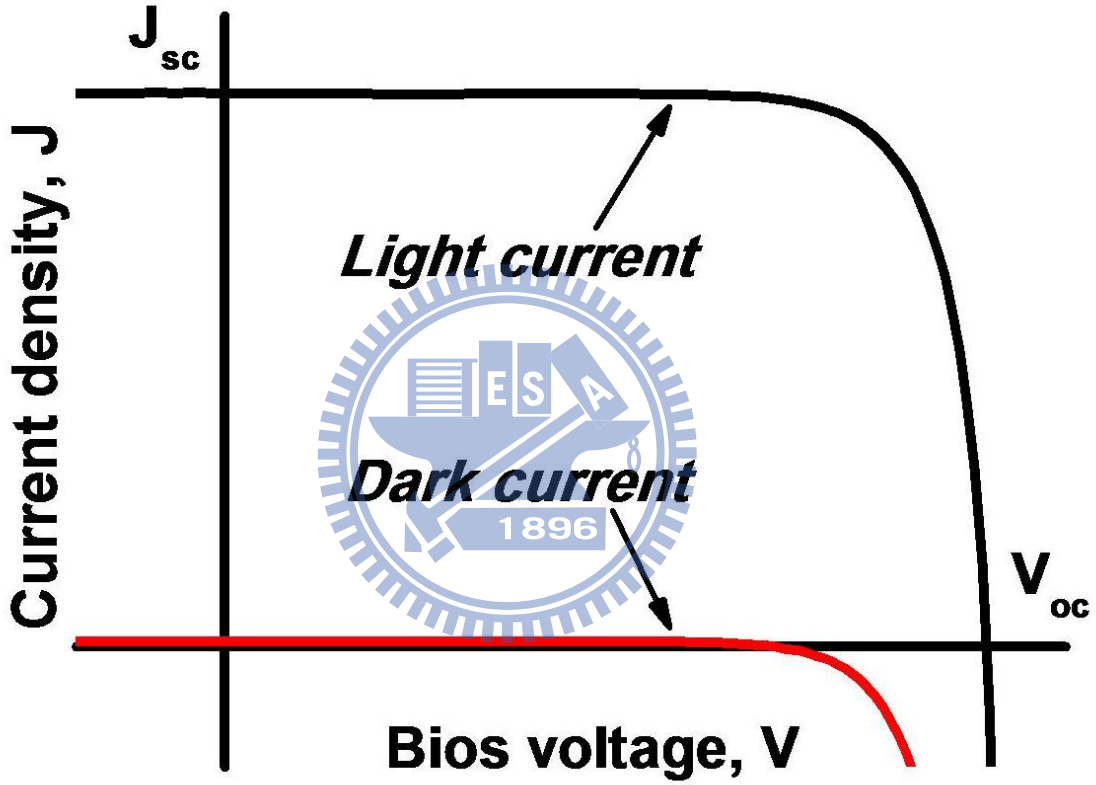

Figure 2.5 The I-V characteristics with and without illumination.

The I-V characteristics of solar cell in dark condition and under illumination were shown in Figure 2.5 [12]. Four parameters are usually used to characterize the solar cell output performances and shown in this figure. The parameters used to describe the solar cell performances are indicated as follows [13]:

(1) Short-Circuit Current, I_{sc}

I_{sc} is determined on the voltage (V) equal to zero by Eq. (2-2). This is equal to the light-generated current I_L ideally. As V=0, the Eq. (2-2) can be written as:

$$I = I_{sc} \tag{2-5}$$

(2) Open-Circuit Voltage, V_{oc}

The open-circuit voltage V_{oc} can be solved in I=0 and V=V_{oc} from Eq. (2-2), which is expressed as:

$$V_{oc} = \frac{nkT}{q} \ln\left(\frac{I_{sc}}{I_0} + 1\right) \tag{2-6}$$

V_{oc} is determined by the properties of the semiconductor by virtue of its dependence on I_0.

(3) Fill Factor, FF

Which is defined as the maximum ratio of the output power to the product on the short-circuit current and open-circuit voltage, which can be expressed as:

$$FF \equiv \frac{I_{max} \times V_{max}}{I_{sc} \times V_{oc}} = \frac{P_{max}}{I_{sc} \times V_{oc}} = 1 - \frac{kT}{qV_{oc}} \ln\left(1 + \frac{qV_{max}}{kT}\right) - \frac{kT}{qV_{oc}} \tag{2-7}$$

It is measure of how squareness the output characteristics are. For cell of reasonably efficiency, it has a value in the range 0.7 to 0.85.

(4) Conversion Efficiency, η

The conversion efficiency of solar cell is defined as the maximum ratio of the output power to the input power, which can be expressed as

$$\eta = \frac{P_{max}}{P_{in}} = \frac{I_{max} \times V_{max}}{P_{in}} = \frac{I_{sc} \times V_{oc} \times FF}{P_{in}} = \frac{I_L \times \left[1 - \frac{kT}{qV_{oc}} \ln\left(1 + \frac{qV_{max}}{kT}\right) - \frac{kT}{qV_{oc}}\right]}{P_{in}} \quad (2\text{-}8)$$

where P_{in} is the total power under the light incident to the cell.

The solar cell parameters such as open-circuit voltage V_{oc}, short-circuit current I_{sc} and fill factor FF can provide the information about designing and improving the photodiode due to their characteristics depended on the properties of the semiconductor materials and the structure of device.

(5) Quantum Efficiency

Quantum efficiency (QE) is the ratio of the number of charge carriers collected by the solar cell to the number of photons of a given energy shining on the solar cell. QE therefore relates to the response of a solar cell to the various wavelengths in the spectrum of light shining on the cell. The QE is given as a function of either wavelength or energy. If all the photons of a certain wavelength are absorbed and we collect the resulting minority carriers (for example, electrons in a p-type material), and then the QE at that particular wavelength has a value of one. The QE for photons with energy below the bandgap is zero.

The quantum efficiency ideally has a square shape, where the QE value is fairly constant across the entire spectrum of wavelengths measured. However, the QE for most solar cells is reduced because of the effects of recombination, where charge carriers are not able to move into an external circuit. The same mechanisms that affect the collection probability also affect the QE. For example, modifying the front surface can affect carriers generated near the surface. And because high-energy (blue) light is absorbed very close to the surface,

considerable recombination at the front surface will affect the "blue" portion of the QE. Similarly, lower energy (green) light is absorbed in the bulk of a solar cell, and a low diffusion length will affect the collection probability from the solar cell bulk, reducing the QE in the green portion of the spectrum. In somewhat technical terms, the quantum efficiency can be viewed as the collection probability due to the generation profile of a single wavelength, integrated over the device thickness and normalized to the number of incident photons.

"Quantum efficiency" is also sometimes called IPCE, which stands for Incident-Photon-to-electron Conversion Efficiency.

Two types of quantum efficiency (QE) of a solar cell are often considered:

- External Quantum Efficiency (EQE) is the ratio of the number of charge carriers collected by the solar cell to the number of photons of a given energy shining on the solar cell from outside (incident photons).
- Internal Quantum Efficiency (IQE) is the ratio of the number of charge carriers collected by the solar cell to the number of photons of a given energy that shine on the solar cell from outside and are absorbed by the cell.

The IQE is always larger than the EQE. A low IQE indicates that the active layer of the solar cell is unable to make good use of the photons. A low EQE can indicate that, but it can also, instead, indicate that a lot of the light was reflected.

To measure the IQE, one first measures the EQE of the solar device, then measures its transmission and reflection, and combines these data to infer the IQE.

(6) Parasitic Resistances

In real cells power is dissipated through the resistance of the contacts and through leakage currents around the sides of the device. These effects are equivalent electrically to two parasitic resistances in series (R_s) and in parallel (R_{sh}) with the cell (Figure 2.4).

The series resistance arises from the resistance of the cell material to current flow, particularly through the front surface to the contacts, and from resistive contacts. Series resistance is a particular problem at high current densities, for instance under concentrated light. The parallel or shunt resistance arise from leakage of current through the cell, around the edges of the device and between contacts of different polarity. It is a problem in poorly rectifying devices.

Series and parallel resistance reduce the fill factor as shown in Figure 2.6. For an efficient cell we want R_s to be as small and R_{sh} to be as large as possible.

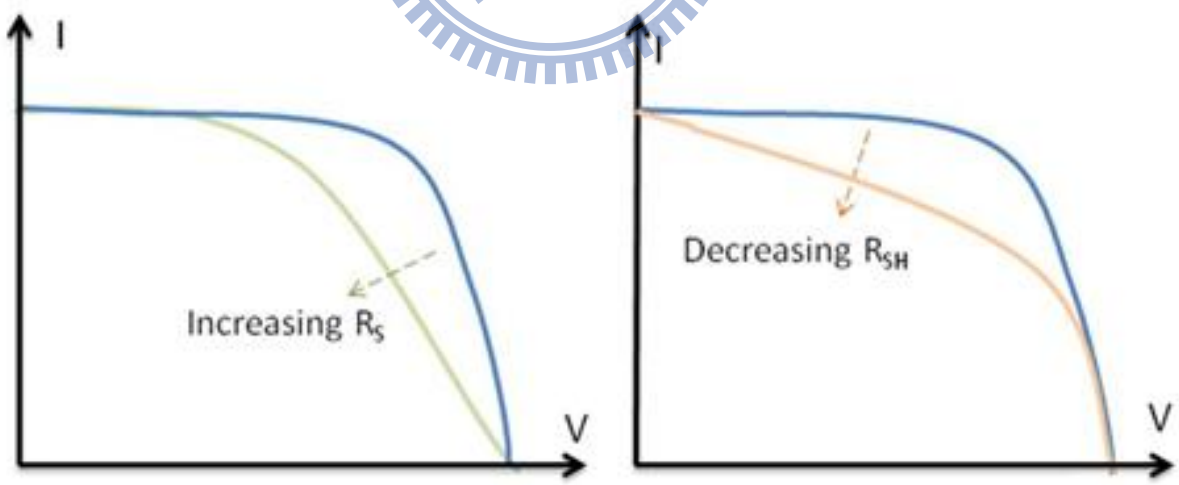

Figure 2.6 Effect of increasing series and reducing parallel resistances. In each case the outer curve has $R_s = 0$ and $R_{sh} = \infty$. In each case the effect of the resistances is to reduce the area of the maximum power rectangle compared to $J_{sc} \times V_{oc}$.

Ⅲ. Experimental and Measuring Instruments

3.1 Plasma-enhanced chemical vapor deposition (PECVD)

Plasma-enhanced chemical vapor deposition (PECVD) is a process used to deposit thin films from a gas state (vapor) to a solid state on a substrate. Chemical reactions are involved in the process, which occur after creation of a plasma of the reacting gases. The plasma is generally created by RF (AC) frequency or DC discharge between two electrodes, the space between which is filled with the reacting gases.

Plasma deposition is often used in semiconductor manufacturing to deposit films onto wafers containing metal layers or other temperature-sensitive structures. Silicon dioxide can be deposited from dichlorosilane or silane and oxygen, typically at pressures from a few hundred millitorr to a few torr. Plasma-deposited silicon nitride, formed from silane and ammonia or nitrogen, is also widely used, although it is important to note that it is not possible to deposit a pure nitride in this fashion. Plasma nitrides always contain a large amount of hydrogen, which can be bonded to silicon (Si-H) or nitrogen (Si-NH); this hydrogen has an important influence on UV absorption, stability, mechanical stress, and electrical conductivity.

Silicon Dioxide can also be deposited from tetraethoxysilane (TEOS) in an oxygen or oxygen-argon plasma. These films can be contaminated with significant carbon and hydrogen as silanol, and can be unstable in air. Pressures of a few torr and small electrode spacings, and/or dual frequency deposition, are helpful to achieve high deposition rates with good film stability.

High-density plasma deposition of silicon dioxide from silane and oxygen/argon has been widely used to create a nearly hydrogen-free film with good conformality over complex surfaces, the latter resulting from intense ion bombardment and consequent sputtering of the deposited molecules from vertical onto horizontal surfaces [14].

3.2 Scanning electron microscope (SEM)

A scanning electron microscope (SEM) is a type of electron microscope that images a sample by scanning it with a high-energy beam of electrons in a raster scan pattern. The electrons interact with the atoms that make up the sample producing signals that contain information about the sample's surface topography, composition, and other properties such as electrical conductivity.

The types of signals produced by an SEM include secondary electrons, back-scattered electrons (BSE), characteristic X-rays, light (cathodoluminescence), specimen current and transmitted electrons. Secondary electron detectors are common in all SEMs, but it is rare that a single machine would have detectors for all possible signals. The signals result from interactions of the electron beam with atoms at or near the surface of the sample. In the most common or standard detection mode, secondary electron imaging or SEI, the SEM can produce very high-resolution images of a sample surface, revealing details less than 1 nm in size. Due to the very narrow electron beam, SEM micrographs have a large depth of field yielding a characteristic three-dimensional appearance useful for understanding the surface structure of a sample. This is exemplified by the micrograph of pollen shown to the right. A wide range of magnifications is possible, from about 10 times (about equivalent to that of a powerful hand-lens) to more than 500,000 times, about 250 times the magnification limit of

the best light microscopes. Back-scattered electrons (BSE) are beam electrons that are reflected from the sample by elastic scattering. BSE are often used in analytical SEM along with the spectra made from the characteristic X-rays. Because the intensity of the BSE signal is strongly related to the atomic number (Z) of the specimen, BSE images can provide information about the distribution of different elements in the sample. For the same reason, BSE imaging can image colloidal gold immuno-labels of 5 or 10 nm diameter which would otherwise be difficult or impossible to detect in secondary electron images in biological specimens. Characteristic X-rays are emitted when the electron beam removes an inner shell electron from the sample, causing a higher energy electron to fill the shell and release energy. These characteristic X-rays are used to identify the composition and measure the abundance of elements in the sample [15].

3.3 Transmission electron microscopy (TEM)

Transmission electron microscopy (TEM) is a microscopy technique whereby a beam of electrons is transmitted through an ultra thin specimen, interacting with the specimen as it passes through. An image is formed from the interaction of the electrons transmitted through the specimen; the image is magnified and focused onto an imaging device, such as a fluorescent screen, on a layer of photographic film, or to be detected by a sensor such as a CCD camera.

TEMs are capable of imaging at a significantly higher resolution than light microscopes, owing to the small de Broglie wavelength of electrons. This enables the instrument's user to examine fine detail—even as small as a single column of atoms, which is tens of thousands times smaller than the smallest resolvable object in a light microscope. TEM forms a major

analysis method in a range of scientific fields, in both physical and biological sciences. TEMs find application in cancer research, virology, materials science as well as pollution, nanotechnology, and semiconductor research.

At smaller magnifications TEM image contrast is due to absorption of electrons in the material, due to the thickness and composition of the material. At higher magnifications complex wave interactions modulate the intensity of the image, requiring expert analysis of observed images. Alternate modes of use allow for the TEM to observe modulations in chemical identity, crystal orientation, electronic structure and sample induced electron phase shift as well as the regular absorption based imaging.

The first TEM was built by Max Knoll and Ernst Ruska in 1931, with this group developing the first TEM with resolving power greater than that of light in 1933 and the first commercial TEM in 1939 [16].

3.4 Integrating sphere reflectance measurement

Figure 3.1(A) is a traditional reflectivity measurements diagram. When we want to measure the reflectance of the smooth surface, the laser light is incident to the sample surface by a specific angle. As the sample itself is a smooth surface, and the incident light is single wavelength, we can obtain the reflected light at corresponding angle by the Snell's law. At this point we just put on a light detector on the path of the reflected light, and we can collect the reflected light from the sample surface effectively. Thus it can measure the reflectance value.

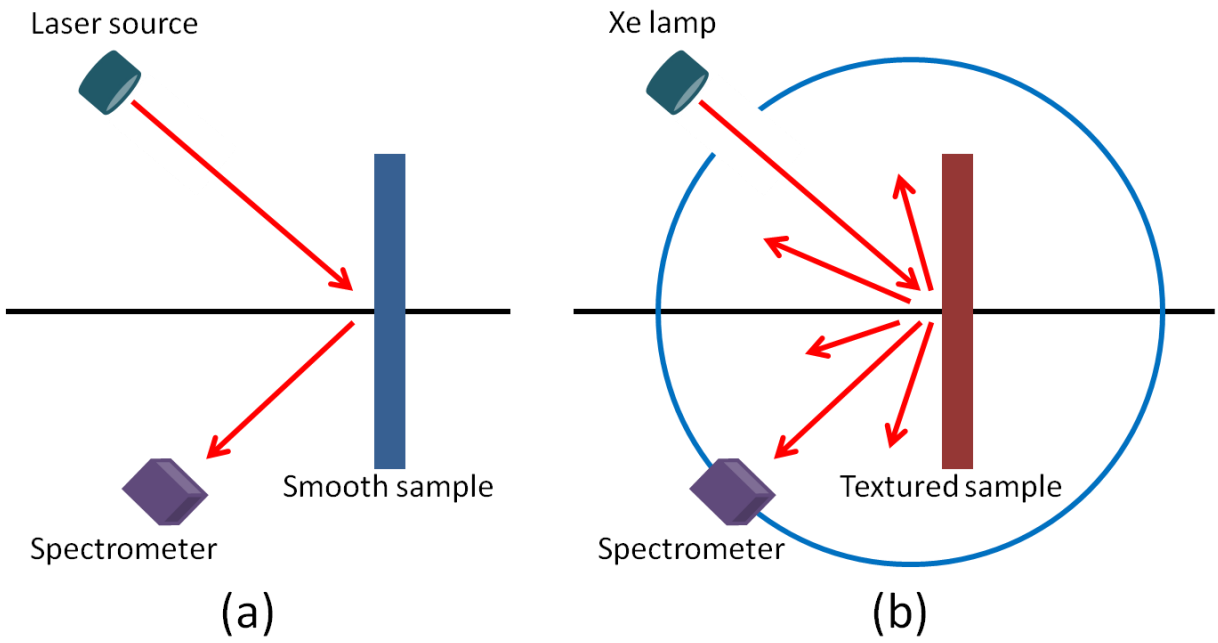

Figure 3.1 (a) Schematic diagram of conventional reflectivity measurements. (b) Schematic diagram of Integrating sphere reflectance measurements.

For the particles surface or rough samples, we also want to understand the different wavelengths light reflectivity, so we change the incident light source to the Xe lamp light with broadband spectrum. Figure 3.1(b) shows, when we made the surface of the textured structure which the dimension size is closed to the wavelength of incident light, the different wavelengths of light on the structure surface produce different levels of splitting, and at the same time with a large number of light diffraction and scattering phenomenon, which will make the direction of reflected light is no longer regularly, but from different angles toward the divergent out. In such condition, if we still use previously measurement way which placed a light detector in a particular direction, we will only receive a small portion of the reflected light, so that out of the reflectance measurement is not an objective value. For rough surface samples, in order to improve the problem of not only received light at a specific point, Fig. 3-1(b), our approach is coupled with an integrating sphere to collect the complete angle scatter light, the light spilling in all directions will be limited to points inside the integrating

sphere and were eventually collected by the light detector. And in order to analyze the reflectivity of different wavelengths, we require a light detector which can detect wide spectrum of light. By this way we obtained an objective of the reflectivity data, which compared to the previous method of measuring reflectivity will be more realistic and accurate.

Figure 3.2 you can see the whole device roughly, we use Xe lamp as the light source to simulate a wide spectrum of solar incident light, then light pass a convex lens by a guiding fiber, this allows light to show about horizontal to pass the aperture of the integrating sphere.

The horizontal light pass the aperture of the integrating sphere then illuminate the sample on the fixture in the integrating sphere. The reflected light is not absorbed by the sample will be limited to points inside the integrating sphere, and then be collected by the light detector at the rear of integrating sphere. This fixture platform can be set around rotating, and we can use this rotating to change the incident light angle of sample illumination. So the angle-resolved reflection of textured sample can be measured by the integrating sphere easily.

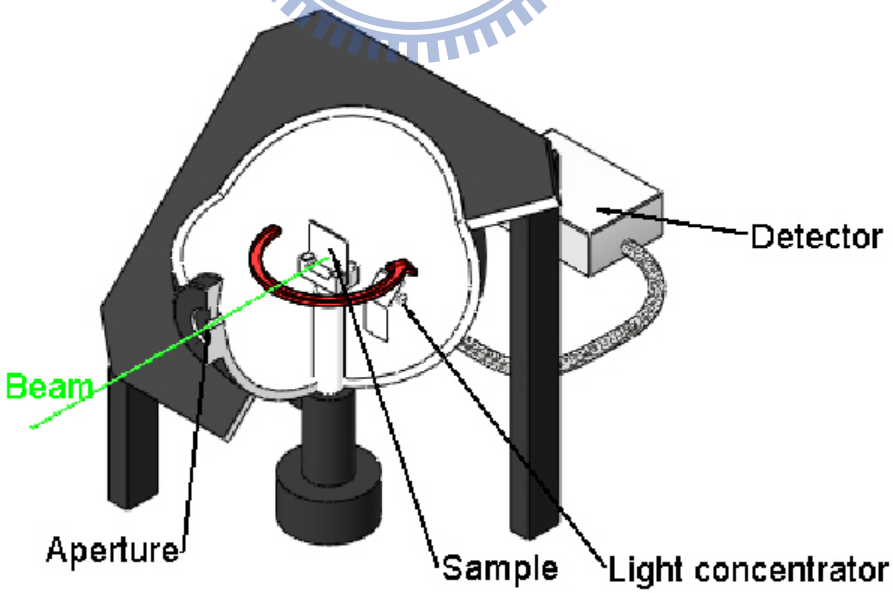

Figure 3.2 Schematic diagram of integrating sphere in our laboratory.

3.5 Power conversion efficiency measurement

Solar cell device characteristics measurement and analysis in the laboratory, set up by self-complete measure machine architecture to achieve. We use the U.S. company manufacturing Newport's AM1.5G 1000W Class A standard solar simulator, the United States National Renewable Energy Laboratory (NREL) calibrated with international standards set by the solar spectrum in all bands are within error of only 2%. Before the actual measurement, using Newport calibration with standard solar cells go after the correction light intensity under the conditions in 1 sun. We use the temperature controller to maintain the temperature of load placed at 25℃. And with a Keithley 2400 digital power meter, through a computer Labview program to control the I-V measurement system. Here is our measuring machine architecture:

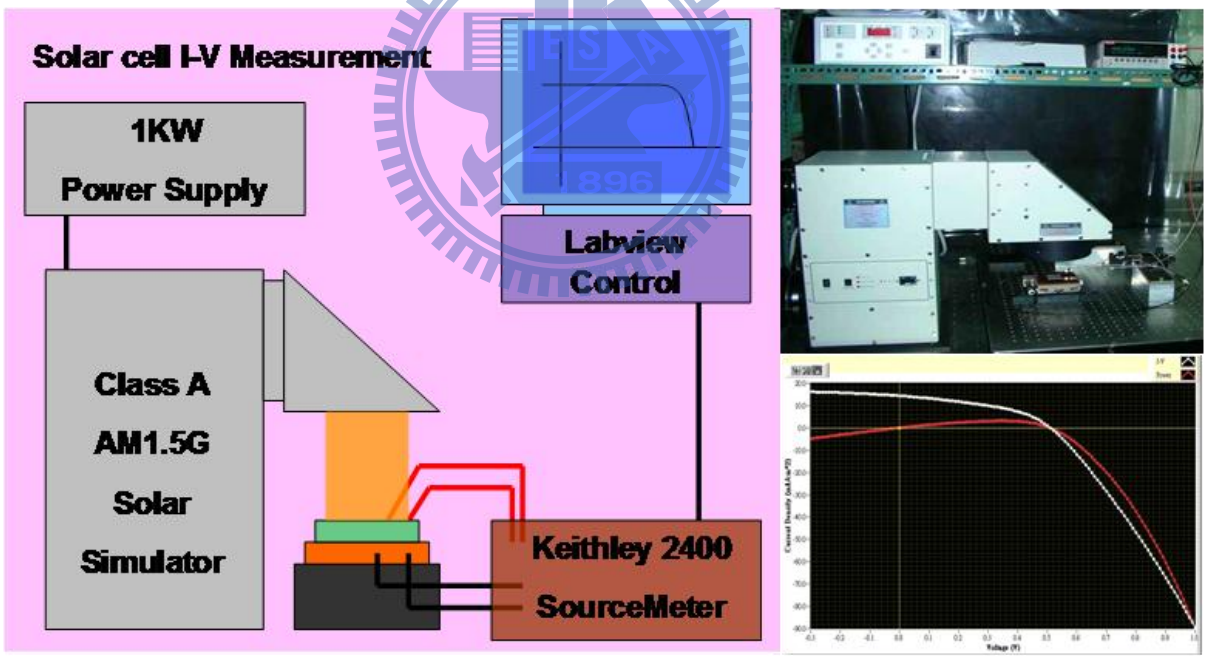

Figure 3.3 Schematic diagram of energy conversion efficiency measurement, including a solar simulator, a Keithley 2400 digital power meter for the measurement of electrical characteristics, and a computer with Labview program to process the measurement data.

Energy conversion efficiency of solar cells is measured the I-V characteristics under simulated sunlight illumination conditions (AM1.5G). We can learn about the important parameters through the conversion efficiency of solar cells, including short-circuit current (I_{sc}), open-circuit voltage (V_{oc}), fill factor (FF), power conversion efficiency (η), Maxima power voltage (V_{max}), Maxima power current (I_{max}), series resistance (R_s), and shunt resistance (R_{sh}).

3.6 External quantum efficiency measurement

The external quantum efficiency (EQE (λ)), also known as spectral response (SR (λ)), is very important to understanding the carrier generation, recombination, and diffusion of photovoltaic devices. External Quantum Efficiency (EQE) is the ratio of the number of charge carriers collected by the solar cell to the number of photons of a given energy shining on the solar cell from outside (incident photons). The unit of frequency response is wattage generated per unit current amperage (A/W), can be converted into quantum efficiency by under equation:

$$QE(\lambda) = \frac{qSR(\lambda)}{\lambda hc} \quad (3\text{-}1)$$

As under the assumption of the short-circuit point is same the maximum power operating point, Frequency response measurement is usually measured in the short-circuit conditions. Solar cell research has developed several sets of external quantum efficiency measurement system, for example: interference filter and grating-based monochrometer. In terms of single junction solar cell, single-frequency light generate optical flow into AC voltage signal and then through the lock-in amplifier to measure. The laboratory uses grating-based monochrometer system, and its set up as Figure 3.4 [17]. It is applicable to broadband spectral measurements (300-1800 nm) and for high spectral resolution. The single-frequency light can

be obtaind by the Xe lamp with broadband spectrum through the grating, and then out from the slit through the monochrometer focused on the solar cell. The problem of aberration can be solve by a spherical mirror or a parabolic mirror.

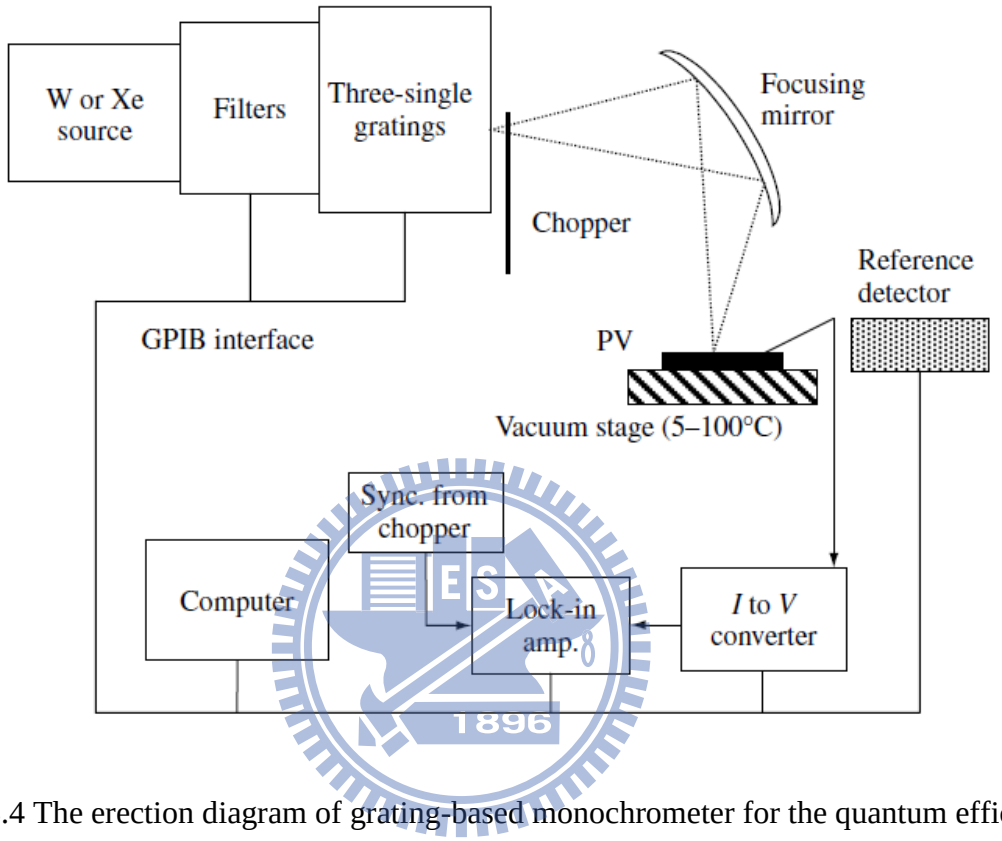

Figure 3.4 The erection diagram of grating-based monochrometer for the quantum efficiency [17].

Ⅳ. Light Management

4.1 Minimizing Reflection

4.1.1 Optical properties of semiconductor

The optical properties of a solid are described by the dielectric constant, ε_s. ε_s is a complex quality and obeys

$$\sqrt{\varepsilon_s} = n_s - ik_s \tag{4-1}$$

where n_s in the refractive index of the material and the imaginary part k_s is related to the absorption coefficient of the material through

$$\alpha = \frac{4\pi k_s}{\lambda} \tag{4-2}$$

In general, ε_s, n_s and k_s are wavelength dependent, and may be direction dependent.

Differences in refractive index determine the reflection and transmission of light at the interface between two materials. For thin films, light should be treated as coherent, and Maxwell's equations can be solved to find the relative amplitudes of transmitted and reflected waves. In the simplest case, that of a plane boundary between materials of refractive index n_0 and n_s, light striking the interface at normal incidence is reflected with probability

$$R = \left(\frac{n_0 - n_s}{n_0 + n_s}\right)^2 \tag{4-3}$$

For a semiconductor, ns is typically 3~4 at visible wavelengths (Table 4.1), so that some 30~40% of light normally incident on the surface from free space will be reflected.

Table 4.1 Refractive indices of selected semiconductors and AR coat materials.

Material	Refractive index (at ca. 1.5 eV)
Si	3.44
Ge	4.00
GaAs	3.6
$Al_{0.8}Ga_{0.2}As$	3.2
AlAs	3.0
Tl_2O_5	2.1
ZnO	2.02
Si_3N_4	1.97
SiO_2	1.46

At oblique incidence the reflectivity is angle and polarization dependent. If the incident ray makes an angle θ_0 with the surface normal, and the transmitted ray an angle θ_s with the surface normal inside the semiconductor then

$$R = \left(\frac{\eta_0 - \eta_s}{\eta_0 + \eta_s}\right)^2 \quad (4\text{-}4)$$

where

$$\eta_s = n_s \sec\theta_s \quad (4\text{-}5)$$

for p polarized light (with the electric field vector in the plane of incidence) and

$$\eta_s = n_s \cos\theta_s \quad (4\text{-}6)$$

and for s-polarized light (electric field vector normal to the plane of incidence). θ_0 and θ_s are related through Snell's law

$$n_0 \sin\theta_0 = n_s \sin\theta_s \quad (4\text{-}7)$$

For unpolarized light, considered as an equal mix of s and p polarizations, the net reflectivity generally increases with angle (for the s polarized component it increase while for the p component it has a minimum), approaching one at large angles. The minimum reflectivity of a semiconductor surface to unpolarized light occurs at normal incidence and is given by Eq. 4-3. At 30~40%, this is unacceptably high for efficient photovoltaic energy conversion.

Snell's law also means that travelling within the semiconductor towards the surface at an angle greater than the critical angle, θ_c, is internally reflected. For an air-semiconductor interface the critical angle is given by

$$\theta_c = \sin^{-1}\left(\frac{n_0}{n_s}\right) \tag{4-8}$$

For the air-silicon interface $\theta_c = 16.9^{\circ}$. In the presence of an optical coating n_0 in Eq. 4-8 is replaced by the refractive index of the coating and θ_c is increased.

4.1.2 Anti-reflection coatings

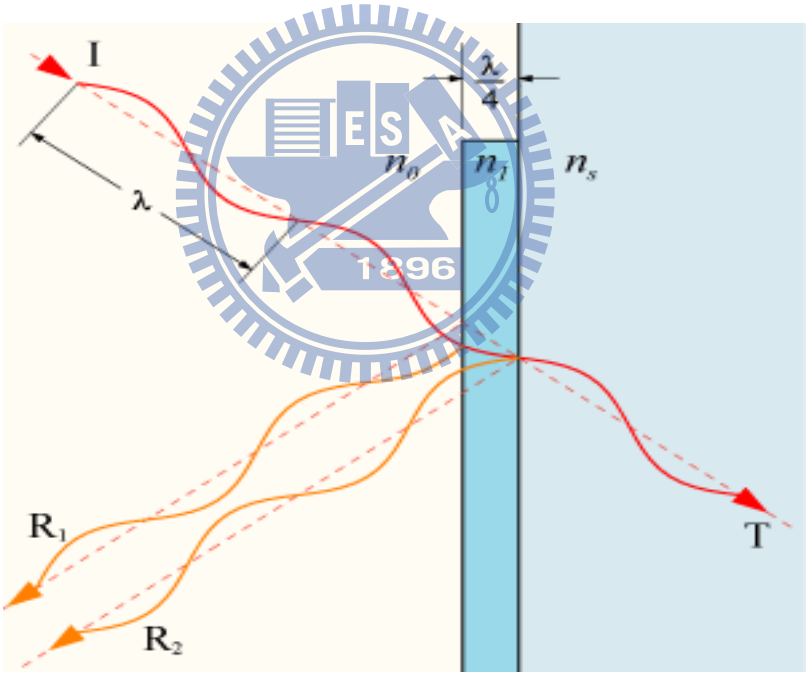

Figure 4.1 Single layer anti-reflection coating. When the thickness of the dielectric layer is equal to one quarter wavelength, the incident and reflected waves interfere destructively to cancel out the reflected ray at the outer surface [18-21].

Reflectivity of the air-semiconductor interface can be reduced using an anti-reflection (AR) coating. An AR coat is a thin film of a dielectric with refractive index n_1 intermediate

between those of the semiconductor (n_s) and free space (n_0). By considering forward and backward travelling waves in each medium it can be shown that the reflectivity of the film for light of wavelength λ is given by

$$R = \frac{(\eta_0-\eta_s)^2+\left(\frac{\eta_0\eta_s}{\eta_1}-\eta_1\right)^2\tan^2\delta_1}{(\eta_0+\eta_s)^2+\left(\frac{\eta_0\eta_s}{\eta_1}+\eta_1\right)\tan^2\delta_1} \quad (4\text{-}9)$$

where δ_1 is the phase shift in the film,

$$\delta_1 = \frac{2\pi\eta_1 d_1 \cos\theta_1}{\lambda} \quad (4\text{-}10)$$

θ_1 is the angle between the light ray and the normal within the film, and d_1 is the film thickness. R clearly has its minimum value when $\delta_1 = \pi/2$. For normal incidence, this first happens when d_1 is equal to a quarter wavelength in the thin film material. (In those conditions the waves reflected from the front and rear interface of the thin film are out of phase and interfere destructively.) R vanishes when it is also true that

$$n_1 = \sqrt{n_0 n_s} \quad (4\text{-}11)$$

So by coating our semiconductor with a thin layer of a medium with refractive index $\sqrt{n_s}$, we can reduce the reflectivity to zero at some particular wavelength, λ_0. Since the solar spectrum is broad, this wavelength should be chosen to lie towards the middle of range of wavelengths which can be usefully absorbed for that semiconductor, and this determines the AR coat thickness. Close to λ_0, R increases with wavelength approximately like $\left(\frac{\Delta\lambda}{\lambda_0}\right)^2$, and at wavelengths where the phase shift becomes a multiple of π, R reaches its maximum value equal to the natural reflectivity of the uncoated interface. This means that an AR coat optimized at one visible wavelength may be quite highly reflecting at others. AR coats on silicon solar cells are usually optimized for red light, where solar irradiance is strong, and become reflective in the blue. For this reason silicon solar cells often appear violet or blue. Similarly, the reflectivity of the AR coat depends on angle, and increase at wide angles. This

means that AR coats are of limited use in diffuse light or for non-planar surface. Figure 4.2 shows how an AR coat which is tuned for normal incidence at a certain wavelength becomes reflecting at other wavelengths and angles.

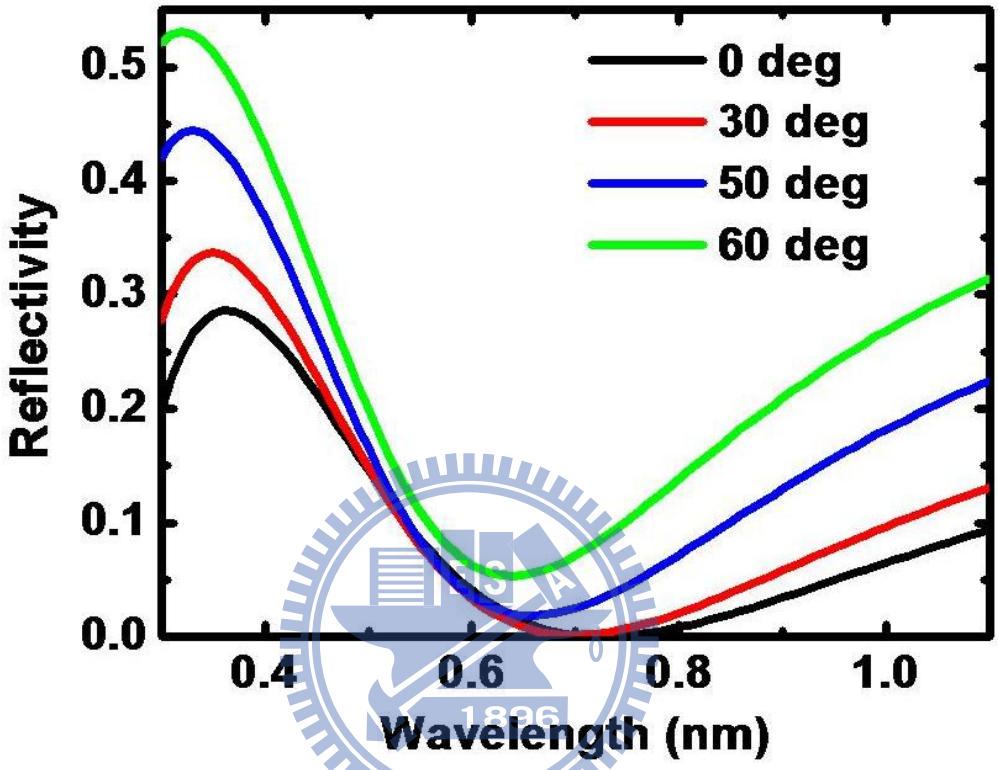

Figure 4.2 Calculated reflectivity of single layer AR coat as function of wavelength at different angles of incidence θ = 0°, 30°, 60°. Notice how the minimum of reflectivity lifts and shifts to shorter wavelengths at wider angles of incidence. Calculated for a 100 nm layer of refractive index $n_1 = \sqrt{3.3}$ on top of a semiconductor of refractive index n_s = 3.3.

In the above treatment of AR coats, we neglect the absorption of the optical materials. This is usually a good approximation since, for most semiconductor, the absorption visible wavelength is sufficiently weak that $k_s \ll n_s$. For reflection from an absorbing medium, n_s should properly be replaced by the complex refractive index $n_s - ik_s$ in Eqs. 4-5~4-9 and R calculated with complex arithmetic. The incident medium should of course be non-absorbing.

According to Eq. 4-11, the ideal AR coat material for silicon should have a refractive index of around 1.84, and for GaAs, 1.90. Good materials are silicon nitride which has n_1 = 1.97 and tantalum oxide with n_1 = 2.1. These give relectivities of less than 1% at normal incidence at the optimum wavelength.

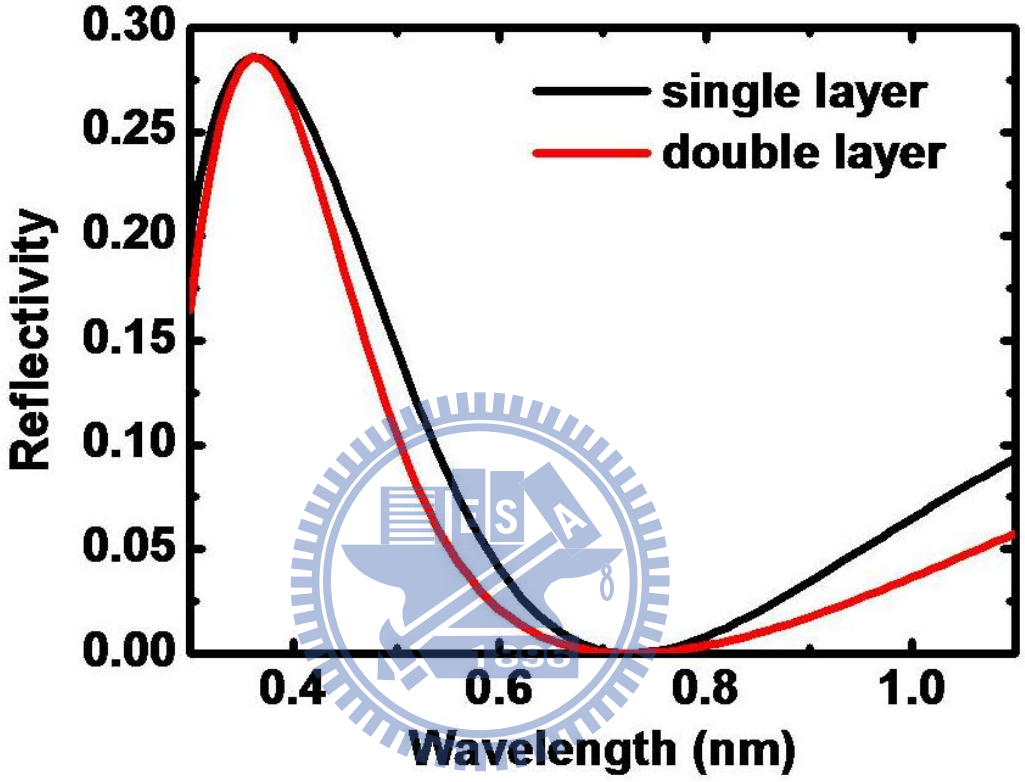

Figure 4-3 Calculated reflectivity of double layer AR coat, optimized for 700nm. The reflectivity of a single layer is presented for comparison.

Improved reflectivity over a band of wavelengths can be achieved with two or more thin films. The greater the number of layers, the greater the range of wavelengths over which the reflectivity can be minimized. Multiple layers are not usually practical for solar cells, given their cost and the sensitivity to angle of incidence, but double layers are used on some hith efficiency cells. Layers should be deposited so that refractive index increases consecutively from air (n_0) to first coat (n_1) to second coat (n_2) to semiconductor (n_s). Reflectivity vanishes

when both films have quarter-wave thickness and

$$\left(\frac{n_2}{n_1}\right)^2 = \frac{n_s}{n_0} \tag{4-12}$$

This condition allows a little more flexibility in choice of materials than the single layer case. In some cell designs, where a wide band gap window layer is present for improved carrier collection, a double layer AR coat can be made simply by choosing an optical coating with refractive index n_1 satisfying Eq. 4-12 where n_2 is the refractive index of the window layer, and choosing appropriate thicknesses. This has been done with GaAs devices having a high aluminium content AlGaAs window. [6]

4.2 Light confinement

In contrast to anti-reflection coats, which increase the fraction of photons admitted to the cell, and concentration which increase the incident flux, light confinement techniques increase the path length of photons inside the cell, once admitted. Increasing the path length increases the probability of photogeneration per incident photon, particularly when the absorption coefficient is small, increasing the absorbed fraction. Light trapping is normally considered in the regime of geometrical optics where structures are large compared to the coherence length of the light, and light rays with different history do not interfere. This is a good approximation in silicon where cells are hundreds of microns thick. In micron scale structures, light should be treated as coherent and interference becomes important. In such systems, classical ray tracing approaches are not valid, and the photogeneration rate must be found from the gradient of the Poynting vector.

The simplest light trapping scheme is to introduce an optical mirror at the rear surface of the cell, either by metallising the rear cell surface or by growing the active layers on top of a Bragg stack. The mirror typically reflects over 95% of rays striking the rear surface. Rays which subsequently reach the front, semiconductor-air, surface are likely to pass through since the reflectivity of that interface must be small for efficient light capture. So the rear mirror effectively doubles the path length of the light. For an ideal mirror (with R = 1) and ideal front surface (with R = 0) the path length is 2w.

The simplest is where one surface is tilted relative to the other. Consider a rear surface tilted at an angle θ_{tilt} relative to the planar front surface, as in Figure 4.4. When $\theta_{tilt} > 1/2*\theta_c$, normally incident rays will be reflected from the rear surface at an angle greater than θ_c, and be totally reflected at the front. If a ray strikes the same portion of the rear surface on the second pass, it will be reflected at an even wider angle, and trapped again. For uniform cell width, both positive and negative tilt angles must be present, so that trapped rays will eventually be reflected at narrower angles and escape. If the positive and negative tilt angles are equal, then each ray makes a multiple of four passes across the cell.

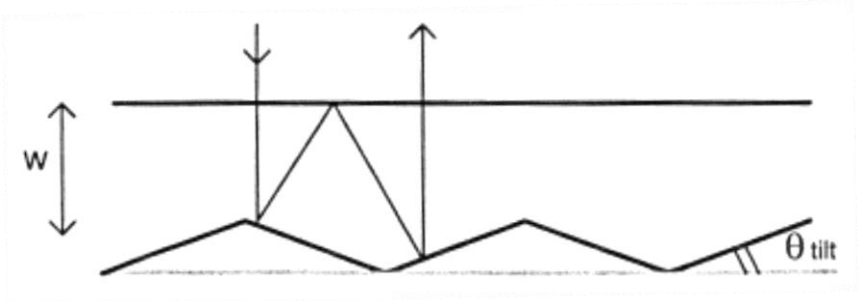

Figure 4.4 Light trapping structure with a tilted rear surface, illustrating a ‘double bounce’ light path. [6]

Ⅴ. Rigorous Coupled-Wave Analysis Method [22]

The diffraction of electromagnetic waves on periodic structures is an important problem with numerous physical and engineering applications. The core algorithm, which is based on Rigorous Coupled-Wave Analysis (RCWA), is a rigorous, fully-vectorial solution of Maxwell's equations [2-2][2-3]. The Rigorous Coupled-Wave Analysis (RCWA) method calculates the diffraction efficiency and field distribution for a 2D or 3D periodic structure. It helps in the design process of applications such as sub-wavelength structures, photonic band gap crystals, and other grating-assisted devices. The RCWA method splits the simulated structure into several parts with optical properties independent in the main propagation direction (i.e., the z direction in this study). Figure 5.1 shows a simple case with only one grating layer. The simulated region is defined by superstrate, grating, and substrate region.

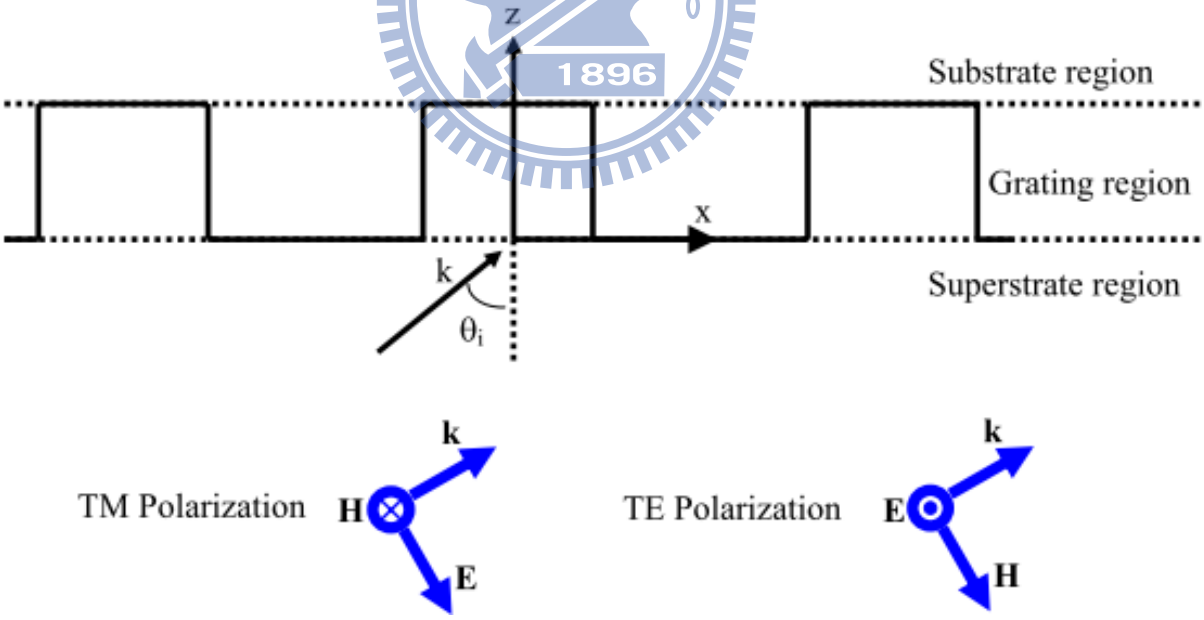

Figure 5.1 The schematic picture of a simple case in the RCWA method. The light is launched from the superstrate region. The analyzed structure is a grating. In the algorithm of RCWA method, all the periodic structures will be split up many such simple grating forms.

By factoring out an assumed time harmonic factor exp(-iωt) , Maxwell's equations can be expressed as:

$$\frac{\partial}{\partial y}E_z - \frac{\partial}{\partial z}E_y = i\omega\mu H_x \tag{5-1}$$

$$\frac{\partial}{\partial z}E_x - \frac{\partial}{\partial x}E_z = i\omega\mu H_y \tag{5-2}$$

$$\frac{\partial}{\partial x}E_y - \frac{\partial}{\partial y}E_x = i\omega\mu H_z \tag{5-3}$$

$$\frac{\partial}{\partial y}H_z - \frac{\partial}{\partial z}H_y = -i\omega\varepsilon E_x \tag{5-4}$$

$$\frac{\partial}{\partial z}H_x - \frac{\partial}{\partial x}H_z = -i\omega\varepsilon E_y \tag{5-5}$$

$$\frac{\partial}{\partial x}H_y - \frac{\partial}{\partial y}H_x = -i\omega\varepsilon E_z \tag{5-6}$$

By substituting Eqs. (5-3)(5-6) into Eqs. (5-1)(5-2)(5-4)(5-5), we derive the following transverse format of Maxwell's equations:

$$\frac{\partial}{\partial z}E_x = \frac{-i}{\omega}\frac{\partial}{\partial x}\frac{1}{\varepsilon}\frac{\partial}{\partial y}H_x + \left(\frac{i}{\omega}\frac{\partial}{\partial x}\frac{1}{\varepsilon}\frac{\partial}{\partial x} + i\omega\mu\right)H_y \tag{5-7}$$

$$\frac{\partial}{\partial z}E_y = \left(\frac{-i}{\omega}\frac{\partial}{\partial y}\frac{1}{\varepsilon}\frac{\partial}{\partial y} - i\omega\mu\right)H_x + \frac{i}{\omega}\frac{\partial}{\partial y}\frac{1}{\varepsilon}\frac{\partial}{\partial x}H_y \tag{5-8}$$

$$\frac{\partial}{\partial z}H_x = \frac{i}{\omega\mu}\frac{\partial}{\partial x}\frac{\partial}{\partial y}E_x + \left(\frac{-i}{\omega\mu}\frac{\partial}{\partial x}\frac{\partial}{\partial x} - i\omega\varepsilon\right)E_y \tag{5-9}$$

$$\frac{\partial}{\partial z}H_y = \left(\frac{i}{\omega\mu}\frac{\partial}{\partial y}\frac{\partial}{\partial y} + i\omega\varepsilon\right)E_x + \frac{-i}{\omega\mu}\frac{\partial}{\partial y}\frac{\partial}{\partial x}E_y \tag{5-10}$$

In order to solve these equations, we need to break the grating structure into simple building blocks with a vertically homogenous region (i.e., a region with value of constant ε in the z direction). A complicated multilayer periodic structure can be decomposed into stacks of such basic building blocks. Then, the RCWA method applies the Fourier wave expansion in a homogeneous layer and Block wave expansion in a periodic structured layer, where has a variation of permittivity in the lateral direction. According to Bloch's Theorem, field components in a periodic layer can be expressed as:

$$E_x = \exp(ik_{x,0}x + ik_{y,0}y)\sum_p \sum_q \exp\left(i\frac{2\pi}{\Lambda_x}px + i\frac{2\pi}{\Lambda_y}qy\right)\sum_m a_{x,m,p,q}[f_m \exp(i\kappa_m z) + g_m \exp(-i\kappa_m z)] \quad (5\text{-}11)$$

$$E_y = \exp(ik_{x,0}x + ik_{y,0}y)\sum_p \sum_q \exp\left(i\frac{2\pi}{\Lambda_x}px + i\frac{2\pi}{\Lambda_y}qy\right)\sum_m a_{y,m,p,q}[f_m \exp(i\kappa_m z) + g_m \exp(-i\kappa_m z)] \quad (5\text{-}12)$$

$$H_x = \exp(ik_{x,0}x + ik_{y,0}y)\sum_p \sum_q \exp\left(i\frac{2\pi}{\Lambda_x}px + i\frac{2\pi}{\Lambda_y}qy\right)\sum_m b_{x,m,p,q}[f_m \exp(i\kappa_m z) - g_m \exp(-i\kappa_m z)] \quad (5\text{-}13)$$

$$H_y = \exp(ik_{x,0}x + ik_{y,0}y)\sum_p \sum_q \exp\left(i\frac{2\pi}{\Lambda_x}px + i\frac{2\pi}{\Lambda_y}qy\right)\sum_m b_{y,m,p,q}[f_m \exp(i\kappa_m z) - g_m \exp(-i\kappa_m z)] \quad (5\text{-}14)$$

The number of expanded waves is theoretically infinite. However, this is impractical in real numerical calculation. The wave expansions have a truncation called the Fourier harmonic number, which indicates the number of the expanded waves to solve the simulation. Then, the |p| and |q| are the integers smaller than the Fourier harmonic number. The complex permittivity of the grating region is also defined by the summation of Fourier series. These waves are coupled to each other and the full vectorial Maxwell's equations to be solved in the Fourier domain. The diffraction efficiencies are then calculated at the end of simulation. The spatial field distribution with each Fourier harmonic number can be derived and then the total electromagnetic field is a sum over these fields. A detail derivation of the RCWA method and its open questions can refer to Ref. [23].

Ⅵ. Application of embedded sub-wavelength substrate on amorphous silicon thin film solar cell

Photovoltaic technology has received increased attention as one of the most promising approach to carbon-free energy production. In recent years, almost 90% of the photovoltaic industry market is dominated by traditional wafer-based silicon solar cells. But the cost of wafer-based silicon solar cells be limited by the cutting technology and is very difficult to reduce. Si-based thin-film solar cells have been a rising star in the photovoltaics industry in the last few years, owing to the advantages of less material usage and large area production [24]. Moreover, using nanostructures is also an appealing solution for increasing performances or lowering manufacturing cost of photovoltaic devices. However, the efficiency of thin film silicon solar cells critically depends on optical absorption in the silicon layer since silicon has low absorption coefficient in the red and near-infrared (IR) wavelength ranges due to its indirect bandgap nature. In typical thin film cells the thickness of the absorbing layer is governed by a tradeoff: the absorber must be optically thick to absorb a significat fraction of the incident photons at the same time the material has to be good enough to enable minority carrier collection lengths larger than the material thickness. These dual requirements largely define the cost per Watt of photovoltaic power. Therefore, for such thin-film structures, shortage of optical absorption length and insufficient optical coupling into the photo-active layer are the major challenges. Efficient light management of reducing the surface reflection as well as increasing the optical path for low energy photons are important, especially in the performance improvement and cost reduction.

In the past, a multilayer antireflection coating (ARC) was commonly used to reduce surface reflection [25][26]. On the other hand, light trapping also provide another method to increase the photon absorption, utilizing geometries to increase the optical path of the photons

near the band edge of the photo-active layer. Conventional light trapping scheme of thin film solar cells focuses on engineering the backside structures, which scatter or diffract the incompletely absorbed photons to oblique angles and hence enhance the propagation length within the absorption layers [27]-[29]. However, the backside structures only passively increase the optical path without the function of antireflection that actively introduce more photons into the cell. Therefore, geometries that simuntaneously reduces the broadband surface reflection and provides light trapping are highly desirable for high efficiency solar cells.

This section describes using the silicon nitride sub-wavelength structure on amorphous silicon solar cell to enhance the light flux, light trapping effect and power conversion efficiency. In traditional fabrication processes, first deposit an ITO layer as the front contact, and the thickness is about 80 nm. This thickness of the ITO layer is for the best anti-reflection effect of thin film at 600 nm wavelength. Sequentially it deposited the p, i, n layers of amorphous silicon on the ITO layer. Finally are another ITO layer as rear contact and an Al metal layer as back reflector. However, these each layer of tradition structure is constituted by flat films, and then it is undesirable of anti-reflection and light trapping effects. Therefore, we hope that a silicon nitride layer is added between the first ITO layer and glass. At the same time we make the sub-wavelength structure on the silicon nitride layer. This can maintain the shape of sub-wavelength structure on the following deposition films. We hope using a structure to meet the function of light trapping and anti-reflection effect. It is expected that this nanostructure can improve the short-circuit current density and power conversion efficiency of solar cells.

We combine both antireflection and light trapping mechanisms by using front pre-patterned nanostructures on the substrate to fabricate a-Si:H solar cells. The pre-patterned nanostructures were fabricated on the SiNx layer utilizing polystyrene (PS) colloidal

lithography, which is suitable for large area production. Then the following standard structures are reproduced layer by layer during the deposition of a-Si:H cells. We believe this novel patterning method is not restricted to a-Si:H solar cells, but is also widely applicable to other thin film materials.

6.1 Fabrication processes

The fabrication of our structure was done on a SiN_x layer deposited on a glass substrate using colloidal lithography followed by a reactive ion etching technique [30]-[33]. The choice of SiNx patterning could function as an index matching layer, while avoid potential damages resulting from patterning the frontal transparent conductive oxide. As illustrated in Figure 6.1(a), a 500 nm thick silicon nitride (SiN_x) layer was first deposited on a glass substrate via plasma-enhanced chemical vapor deposition (PECVD).

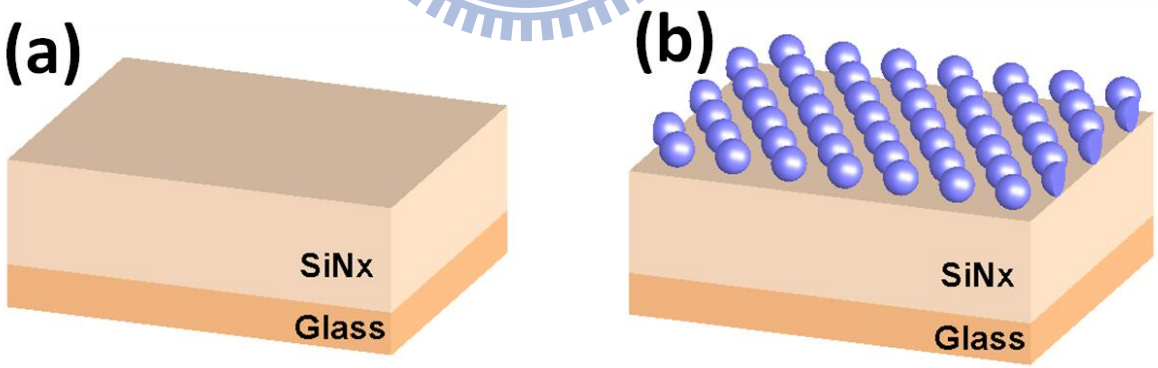

Figure 6.1 In this study, the process of pre-prepared samples. (a) The silicon nitride (SiN_x) of 500 nm was deposited on a glass substrate by using plasma-enhanced chemical vapor deposition (PECVD). (b) The polystyrene (PS) nanospheres was spun on the surface of the SiN_x layer, forming a close-packed monolayer mask, and then shrink the size of the PS spheres.

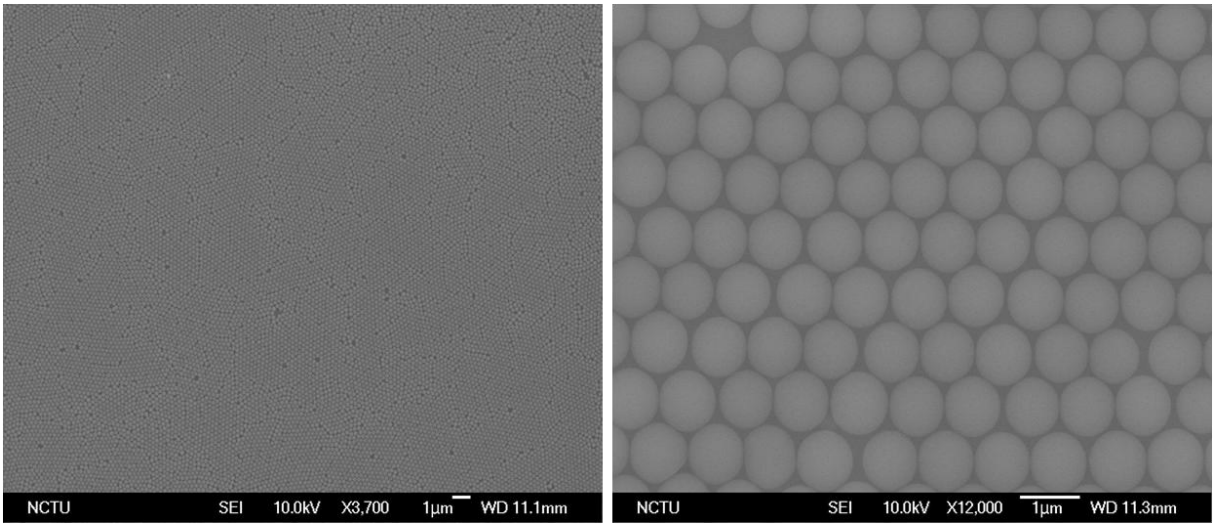

Figure 6.2 The top view SEM images of the closely packed polystyrene nanospheres on the SiN_x layer.

Then, polystyrene (PS) nanospheres with a plurality of 10 wt.% and diameter of 600 nm was spun-coated on the surface of the SiN_x layer, naturally arranging into a closely packed triangular lattice, which served as a self-assembled monolayer mask, and the SEM is shown in the Figure 6.2 [34]-[49]. Subsequently, inductively-coupled-plasma reactive ion etching (ICP-RIE) with incident oxygen (O) plasma was performed to shrink the size of PS spheres in order to facilitate the etching of SiN_x. The flow rate was set to be 20 sccm with a chamber pressure of 0.06 Pa and an RF power of 100 W. It is worth noting that the positions of PS spheres did not change during the size shrinking, as shown in Figure 6.1(b). The separations between PS spheres increased as their sizes decreased. Next, the ICP-RIE was performed on SiN_x and PS spheres with a CHF_3 /O_2 flow rate of 5/5 sccm, a chamber pressure of 1.33 Pa, and an RF power 150 W. The residual PS nanospheres were then removed by dipping into acetone with sonification for 5 min., as schematically shown in Figure 6.3(a). Figures 6.3(b) to 6.3(d) illustrate the deposition of a single-junction a-Si:H solar cell.

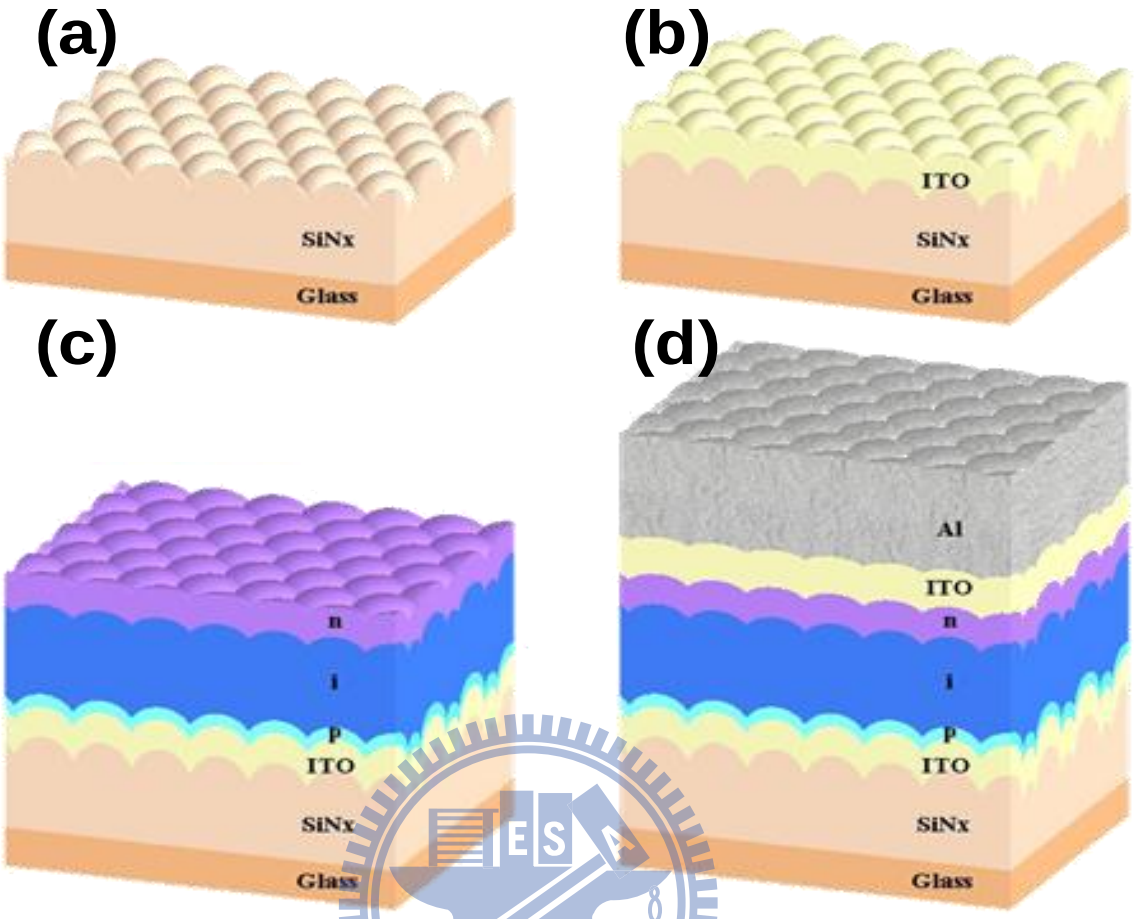

Figure 6.3 The device fabrication process of front pre-pattern substrate a-Si solar cell.

First, an 80 nm thick indium tin oxide (ITO) layer was deposited by DC sputtering. Then, the a-Si:H active layer with a total thickness of 292 nm (p/i/n=12/260/20 nm) was deposited using a high-density-plasma chemical-vapor-deposition (HDP-CVD) system with a growth temperate of 200^{o}C, a constant total pressure at 900 mTorr, and a plasma power density of 0.06 W/cm^{2}. Finally, an 80 nm-thick indium tin oxide (ITO) layer and 500 nm of aluminum were capped on top as the back electrode and reflector. Control cells were also fabricated on a flat glass substrate with a sputtered ITO layer and a commercially available Asahi U-type glass, denoted as the flat and the Asahi U cell, respectively. Figure 6.4(a) is the scanning electron microscopic (SEM) images of the resulting SiNx nipple nanopattern.

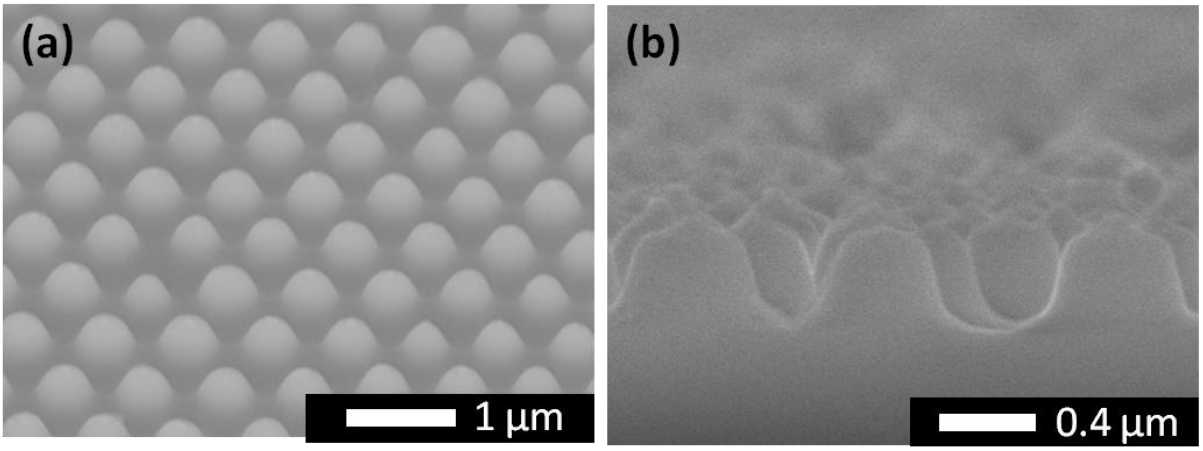

Figure 6.4 Scanning electron microscopic (SEM) images of the fabricated SiNx nipple arrays: (a) a 45-degree tilted top view and (b) a cross-sectional view.

The bottom width and height of nipple pattern can be controlled by varying the etching duration and conditions. As shown in Figure 6.4(b), the height and the bottom width of the patterns are ~450 nm and ~300 nm, respectively. Figure 6.5 shows a cross-sectional transmission electron microscopic (TEM) image of the fully fabricated solar cell on the pre-patterned substrate. The conformal deposition of individual layers is clearly resolved without cracks or voids that could adversely affect the device characteristics.

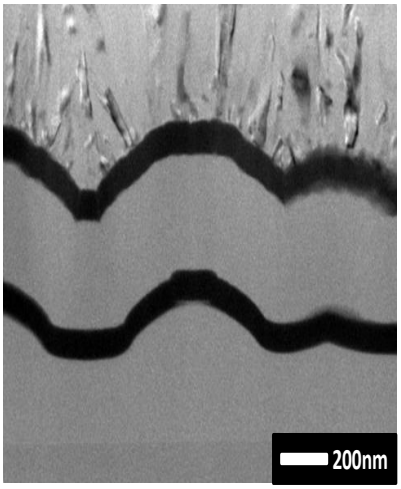

Figure 6.5 The cross-sectional TEM image of a fabricated solar cell on the pre-patterned substrate.

By the way, the commercial Asahi U-type substrate is a simple glass combined with one layer TCO. And the TCO layer is composed of SnO_2:F. However, this type of TCO layer will produce naturally variable degrees of surface roughness during the deposition. And the roughness R.M.S. is about 40nm. The extent of these surface roughnesses is random and not easy to control. The surface SEM image is shown in the Figure 6.6, and Figure 6.7 is the AFM image.

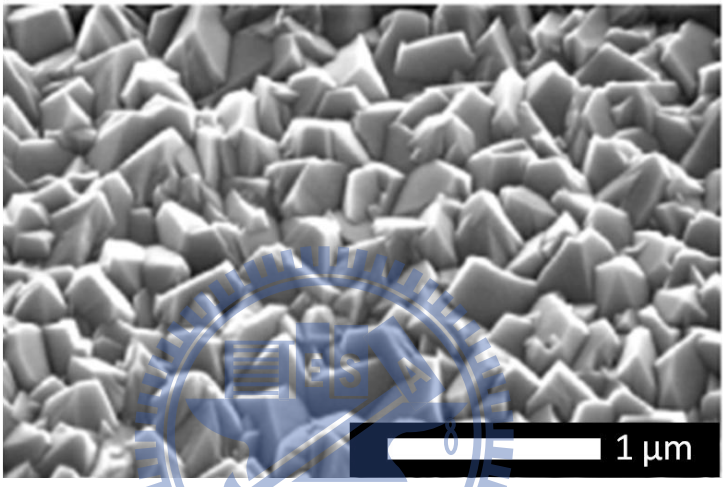

Figure 6.6 SEM image of the Asahi U-type sample

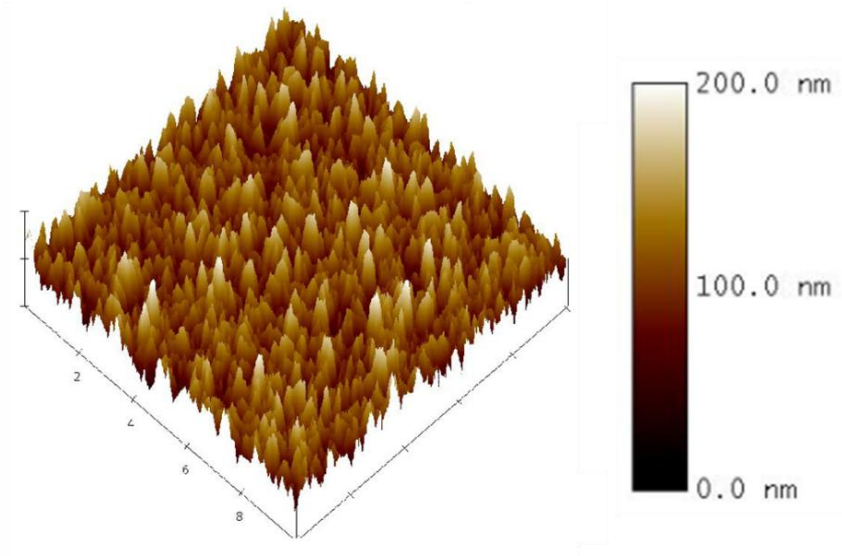

Figure 6.7 AFM image of the Asahi U-type sample

6.2 Experimental results and discussions

Our experiment structure is a embedded front pre-patterned nipple-shaped structure. This structure is mainly expected using the gradient refractive index effect (see Figure 6.6) to achieve anti-reflective and producing light trapping effect at the same time [50]-[56]. The light trapping effect is produced when the light touch to the nano-structure which bring the phenomenon of diffraction and scattering. This can change the travel direction of light and let the light have a longer optical path when it passes in the active layer. At the interface due to the relationship of incident angle is more prone to total reflection, and thus light can be confined to the active layer, to provide more opportunities for long-wavelength light absorption.

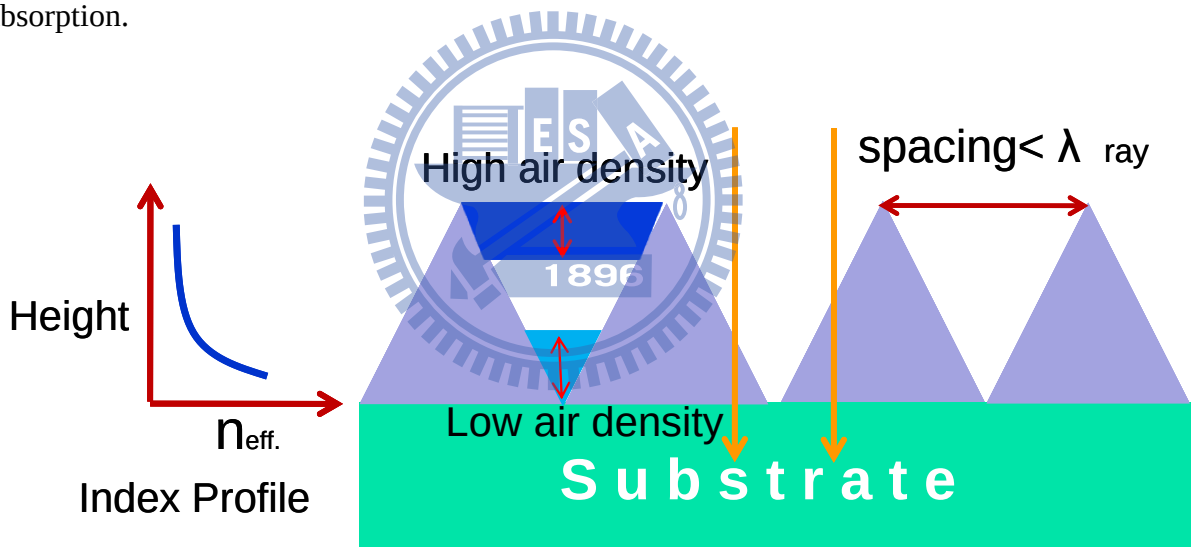

Figure 6.8 Schematic diagram of the sub-wavelength structure for antireflective by gradient refractive index. When the nano-structures is less than the wavelength of incident light, this anti-reflective nano-structure layer can use spatial gradient structure to achieve the effect of graded refractive index. The structure close to the end of air is a higher air ratio and a low refractive index, but the structure close to the end of structure is a lower air ratio and a high refractive index.

6.2.1 Integrating sphere reflectance measurement

To characterize the effects of antireflection and light trapping on these PPS solar cells, this shows the absorption spectrum measured (A=1-R) by an integrating sphere at normal incidence (see Figure 6.7). The cell that utilizes pre-patterned substrate shows superior absorption in the entire spectrum than that of the flat cell. The absorption enhancement is substantially increased in the wavelength range between 600 nm and 800 nm, resulted from the both light trapping and antireflection effects of the pre-patterned substrate. The PPS structure scatters the incident photons and enhances the transmittance of the substrate simutaneously. In addition, the enhanced absorption at the short wavelength range (λ<600nm), is resulted from antireflection effect by the effective refractive index only since the optical length for complete absorption is smaller than the thickness of p-i-n absorber layer.

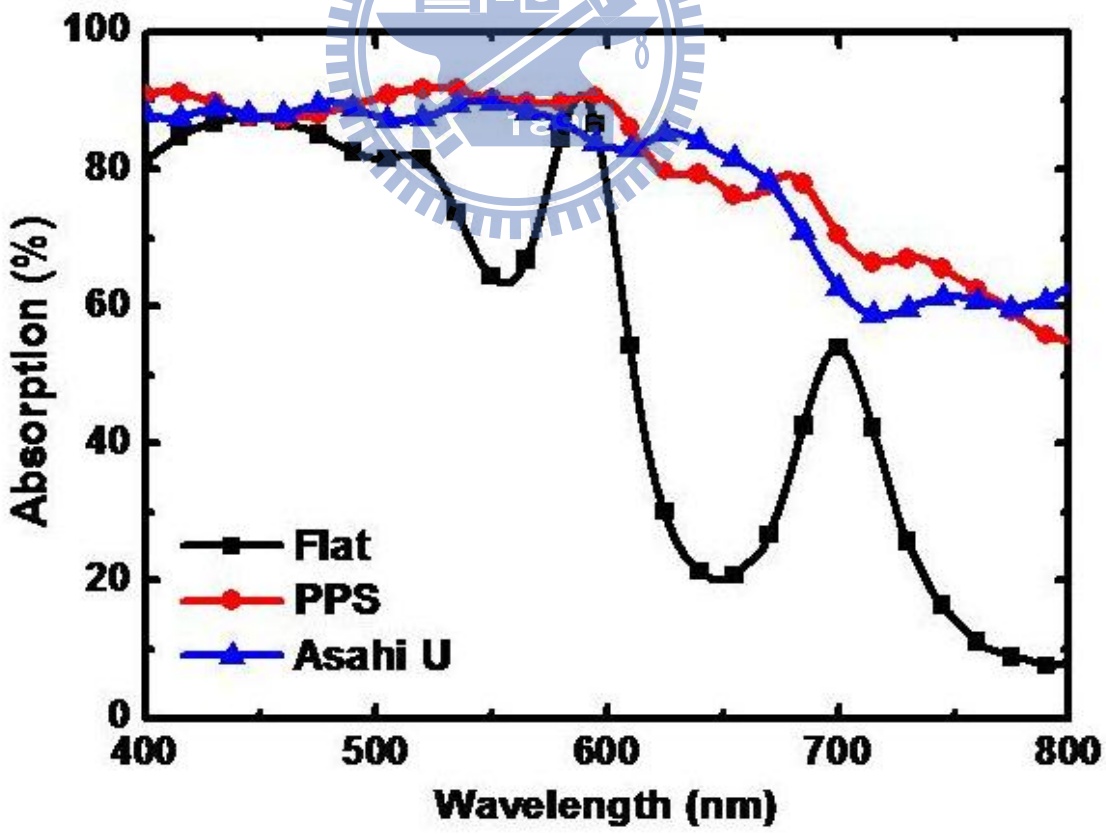

Figure 6.9 The spectrum of cell absorption at normal incident.

6.2.2 External quantum efficiency measurement

Figure 6.8 is the external quantum efficiency (EQE) of three type structures. The EQE enhancement indicates the increased optical absorption. We also can see the enhancement cover most of the solar spectrum that is absorptive to a-Si:H solar cells. The same obvious phenomena of antireflection effect at short wavelength and light trapping at long wavelength also can be found in the EQE spectrum.

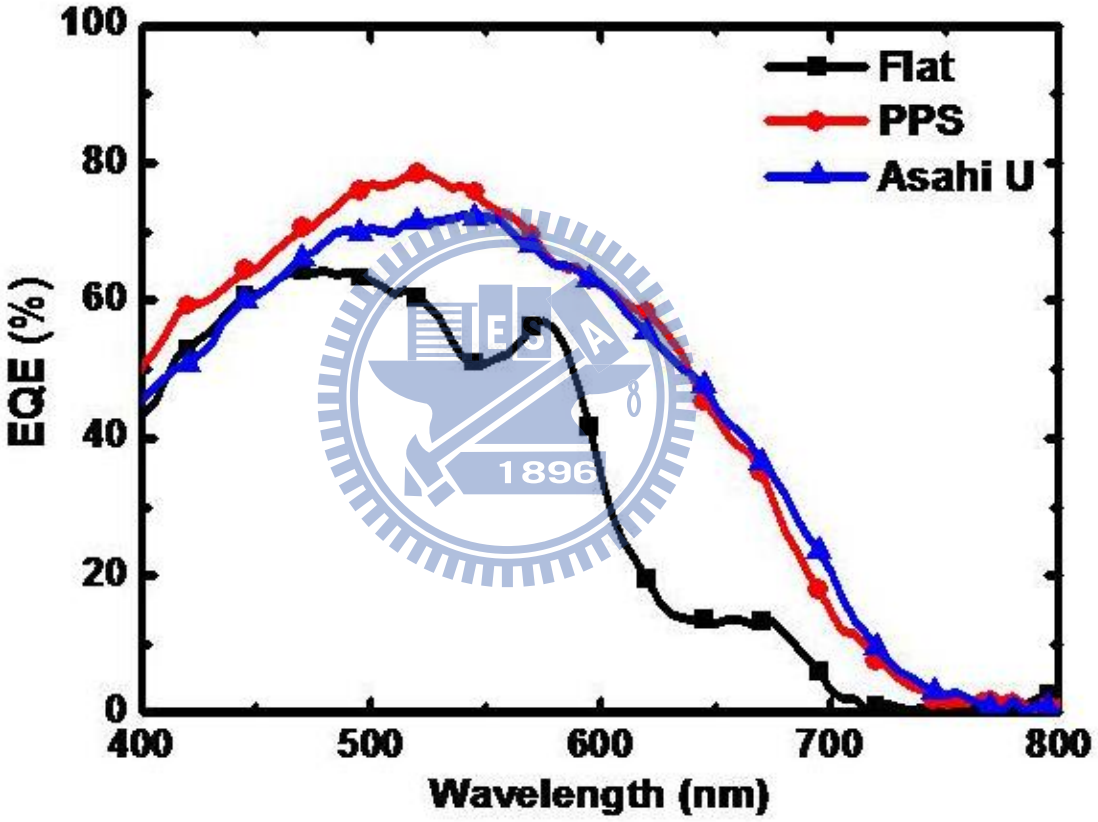

Figure 6.10 The external quantum efficiency (EQE) of the cell for three type substrates.

Figures 6.9(a) and 6.9(b) present the calculated enhancement factors of EQE of textured cells with respect to the flat control cell for wavelengths below and above 600 nm, respectively, where the enhancement factor is defined as $\Delta\ EQE=EQE/EQE_{Flat}$. It can be seen in Figure 6.9(a) that the antireflection property of the PPSs increases the photocurrent

generation by roughly 20% for wavelengths between 400 nm and 575 nm, which is better than the Asahi U cell in this spectral range. For wavelengths longer than 575 nm, the photocurrent generation of the PPS cell achieves 2 to 12-fold enhancements, compared to the control cell, shown in Figure 6.9(b). The significant improvement in the infrared region indicates that the PPS can also effectively enhance the absorption by light trapping as well as the Asahi U.

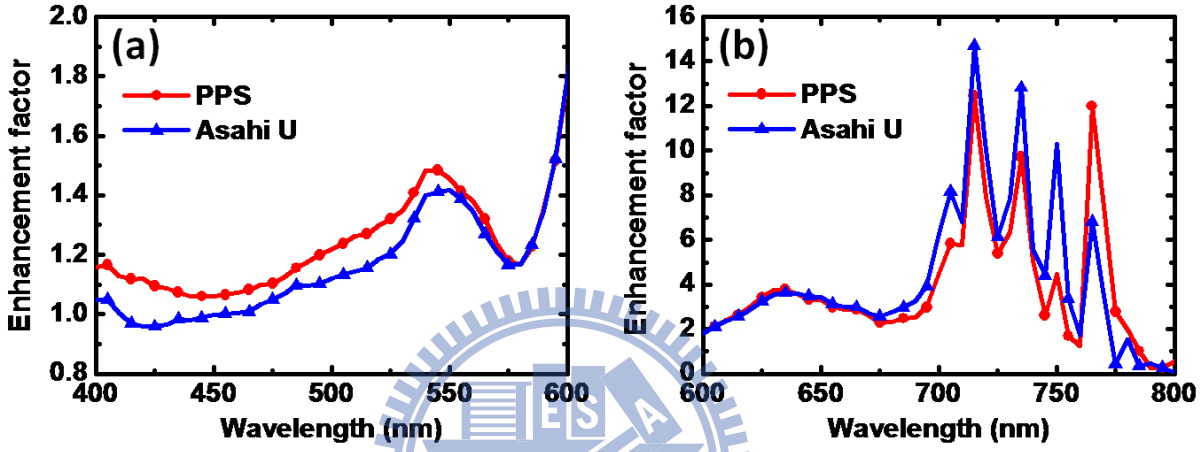

Figure 6.11 The improvement factors of the EQE (Δ *EQE*) for EBN and Asahi U, (a) between 400 nm and 600 nm, and (b) between 600 nm and 800 nm.

Figure 6.12 is the internal quantum efficiency (IQE) of the cell for three type substrates**.** Since we cannot directly measure the IQE of cells, so we obtained the result by through the calculation of EQE/absorption. From the figure, it can be seen that the three types of cells have almost the same IQE in the short wavelength. This situation shows that three components have almost the same growth characteristics of materials. But the flat cell curve has some ripple between the wavelength range of 575nm and 675nm. Speculated that the ripple is caused by the fluctuations of absorption curve, and this may be influenced by the constructive interference or destructive interference of light wave in the glass or SiNx layers.

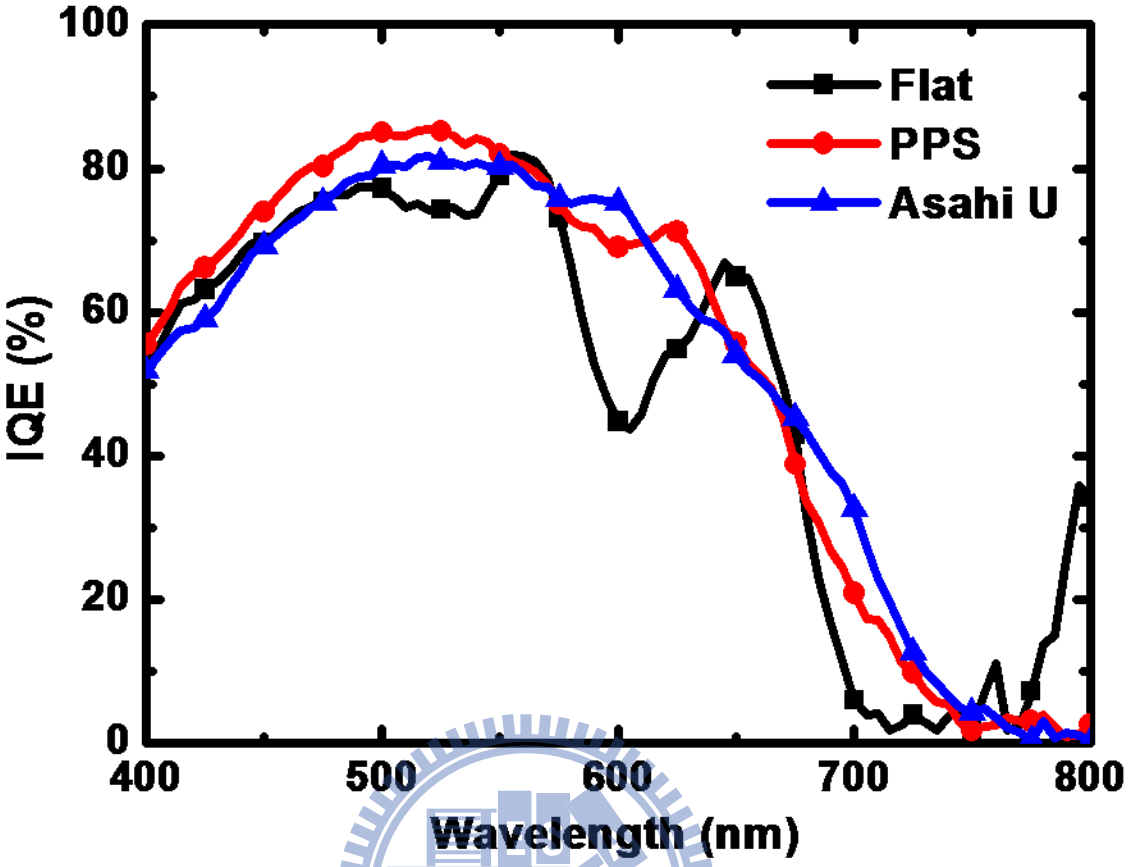

Figure 6.12 The internal quantum efficiency (IQE) of the cell for three type substrates.

6.2.3 Power conversion efficiency measurement

The J-V measurement was performed under a simulated AM1.5G illumination condition (Oriel Class A 1000W) at room temperature following standard calibration and measurement procedures (see Figure 6.10) [57]. The detail electrical information is in the Table 6.1. The open voltage and fill factor for the PPS and flat cell remain aproximately the same. The increased efficiency (from 5.36% to 8.38%) is resulted from the enhanced short-circuit current density (from 12.89 mA/cm^2 to 19.77 mA/cm^2). The PPS cell also shows superior conversion efficiency and current density to the cell that utilized with commerciallized Asahi U-type substrate.

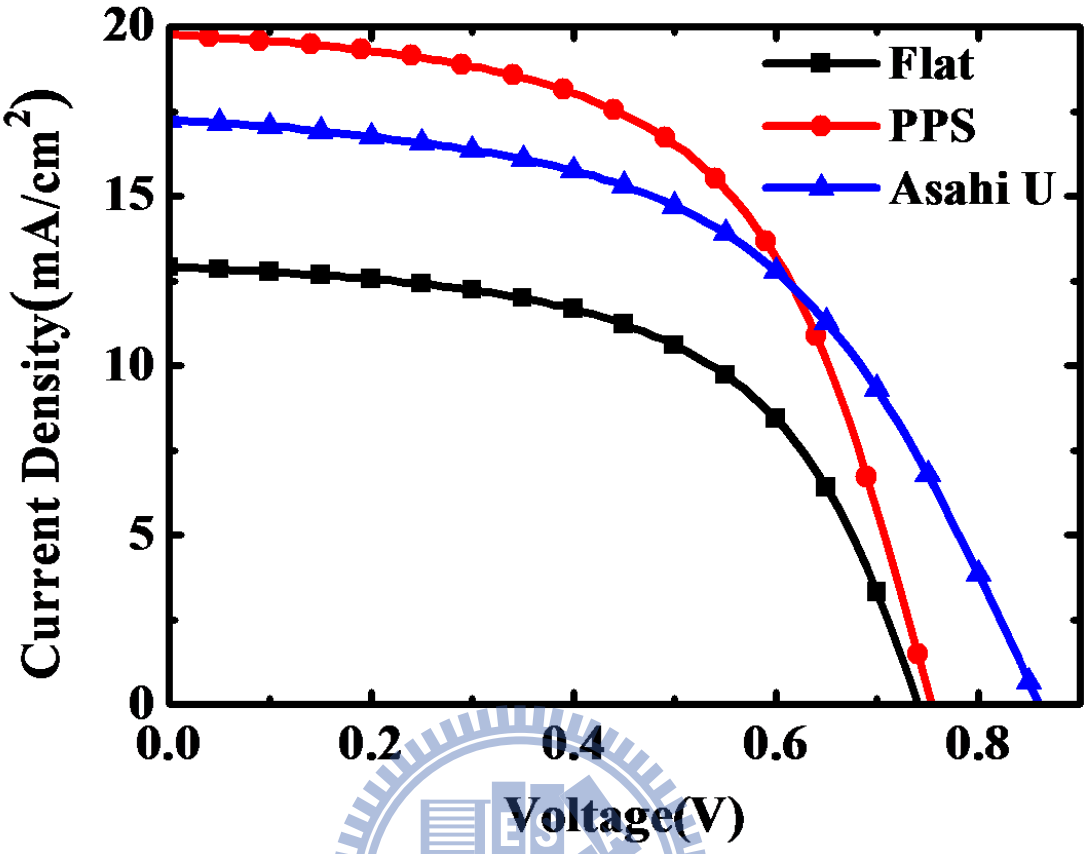

Figure 6.13 J-V measurements of the flat reference, PPS, and Asahi U cells.

Table 6.1 The detail electrical information of J-V measurements.

	Flat	PPS	Asahi U
V_{oc}	0.74	0.75	0.86
J_{sc}	12.89	19.77	17.24
F.F.	56.18	56.25	51.94
η	5.36%	8.38%	7.70%

6.3 Angular absorption

Furthmore, we measured the angle-resolved absorption spectroscopy of the reference flat cell and the PPS cell (see Figure 6.11). From the absorption color maps, it can be clearly seen that the PPS cell exhibits less dependency on wavelengths and incident angles than the flat cells. The PPS structure serves as an omnidirectional antireflective layer, which sufficiently couples the broadband oblique incident waves into the the absorber layer, up to 60°. The results guarantees sufficient light harvesting for the entire day.

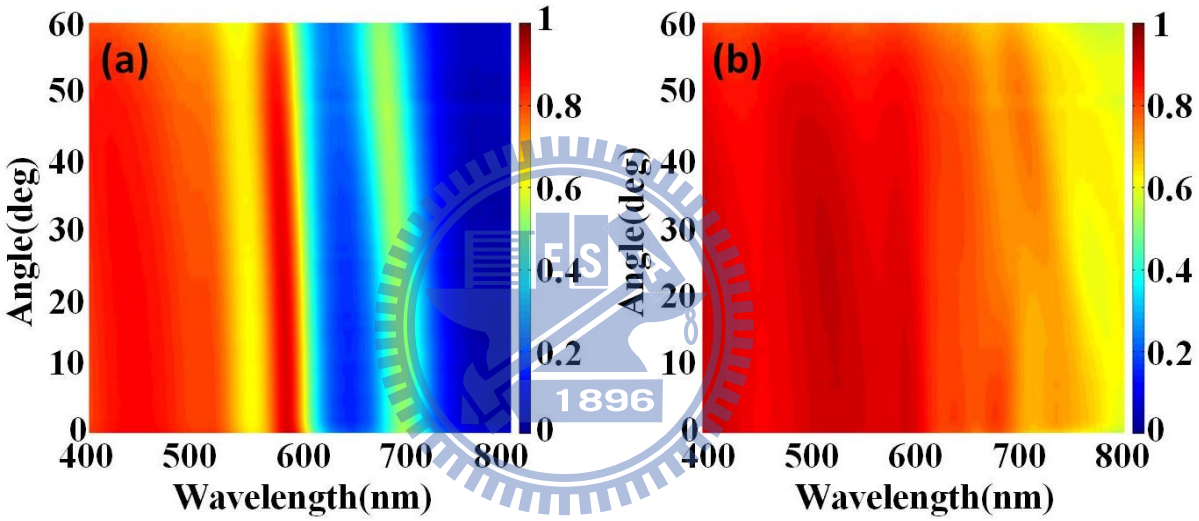

Figure 6.14 The angle-resolved absorption spectroscopy for the cell with the (a) flat substrate and (b) PSS substrate.

6.4 Simulation

We also optimize the frontal pre-patterned substrate structures based on the theoretical calculation using a three-dimensional rigorous coupled wave analysis (RCWA) method. The approach has been utilized to investigate the diffraction and transmission properties of

nano-scale structures. In our simulation, we focus on the optimization of the polystyrene nanospheres of 600 nm period. So the simulated structural parameters include the bottom width and height of SiNx nipple pattern, as shown in Figure 6.12. In the implementation, the bottom width of SiNx nipple pattern can be controlled by the shrink size of the PS spheres before the etching process and the height of SiNx nipple pattern can be adjusted by the etching time.

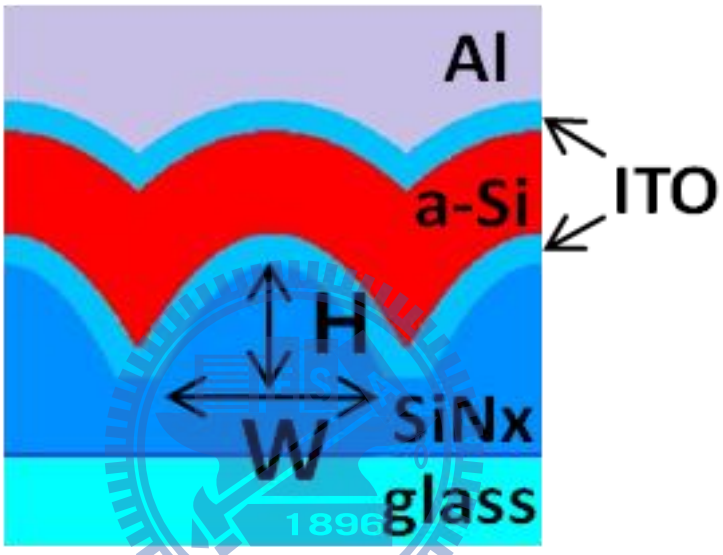

Figure 6.15 The cross section of simulation model structure and the modulation parameters.

The simulated unit cell consists of 3x3 elements in a hexagonal array. Moreover, the material dispersion of each layer is also considered for wavelengths between 300 nm and 800 nm. Accordingly, we calculate the a-Si layer absorption which is a function of the bottom width varying between 400 nm and 600 nm, and the etching height of SiNx nipple pattern from 50 nm to 500 nm. The resulting short-circuit photocurrent (J_{sc}) is calculated using the following equation, taking into account the AM1.5G spectrum and the material response, i.e. internal quantum efficiency:

$$J_{sc} = \frac{e}{hc}\int_{300\ nm}^{800\ nm} \lambda \times IQE(\lambda) \times A_{sim}(\lambda) \times I_{AM1.5G}(\lambda) d\lambda \qquad (6\text{-}1)$$

where $A_{sim}(\lambda)$ denotes the value of calculated absorption.

In the calculation result, we can clearly see that a relative maximum value appearance (see Figure 6.13). The enhancement scale bar is compare with the flat cell current density of simulation. The optimal J_{sc} is obtained for the bottom width and height of 500 nm and 400~450 nm, respectively. According to our previous experimental results, now the height of the actual device patterns is 300 nm and the bottom width of the patterns is 450 nm. Therefore, if the fabrication parameters can be precisely controlled, higher J_{sc} can be obtained by more significant antireflection and light trapping effect. Overall, the simulation technique is powerful and allows customized absorption engineering for solar cells with nanostructures.

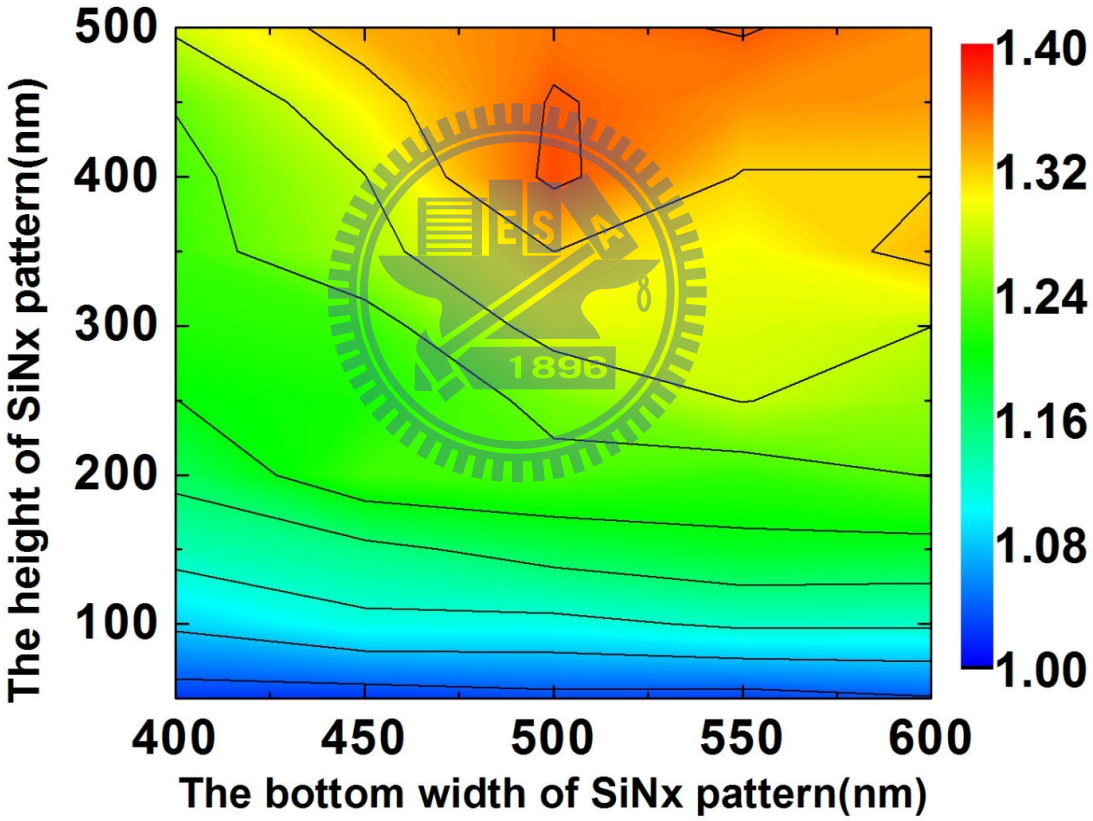

Figure 6.16 The calculated short-circuit current density enhancement compared to the reference flat cell as a function of the bottom width (W) and height (H) of SiNx nipple pattern.

Ⅶ. Conclusion

In summary, we demonstrate a pre-pattern substrate on a-Si thin film solar cells, to serve both anti-reflectance and light trapping. The fabrication of the PSS is based on the colloidal lithography and the reactive-ion etching technique, which is applicable for large area production. The pre-patterned structure embedded in the amorphous materials demonstrates sufficient light coupling at normal incidence, enhancing the photon absorption. The power conversion efficiency of the pre-patterned cell was measured 8.38%, which showed 56.34% and 8.83% enhancement compared to the reference cell with a flat substrate and the commercialized Asahi U-type substrate, respectively. Angle-resolved absorption spectroscopy measurements also show enhanced light coupling to the cells at oblique angle of incidence. This result can directly impact the attainment of scalable renewable energy from a-Si thin-film solar cells. Finally, we obtained the optimized pattern by rigorous coupled wave analysis method. The best structure on our pre-patterned substrate is 500 nm bottom width and 400~450 nm height of SiNx nipple pattern. The resulting light management effects directly enable high-efficiency a-Si:H solar cells and are also broadly applicable to other common thin film solar cells such as poly- and micro-crystalline Si, CdSe, and organic solar cells.

Reference

1. “World energy outlook 2009”, International Energy Agency, 2009.
2. http://encyclobeamia.solarbotics.net/articles/solar_cell.html
3. Martin A. Green, Keith Emery, Yoshihiro Hishikawa and Wilhelm Warta, “solar cell efficiency tables v.35”, Prog. Photovolt: Res. Appl. **18,**144–150 (2010).
4. Marti A. Green, Araujo G. L. “Limiting efficiencies for photovoltaic energy conversion in multigap systems” Solar Energ. Mater. Solar Cells, **43**, 203-222 (1996).
5. Singh. R, “Why silicon is and will remain the dominant photovoltaic material” Journal Of Nanophotonics,**3,** (2009)
6. Jenny Nelson, “The physics of solar cells,” (2003)
7. Jeffery L. Gray, “The Physics of the Solar Cell,” in *Handbook of Photovoltaic Science and Engineering*, John Wiley & Sons, New York, 61-111, (2003).
8. Sze S, *Physics of semiconductor Devices, 3rd Edition*, John Wiley & Sons, New York, 719-741, (2007).
9. S. M. Sze, “Semiconductor Devices Physics and Technology,” (2003)
10. S. S. Chen, “Effects of antireflection coating and prismatic cover on Ⅲ-Ⅴ solar cell performance M. S. Thesis,” CYCU, Taiwan, R.O.C. (2005).
11. 莊家琛,“太陽能工程-太陽能電池篇,” 全華出版社 (2005)
12. M. P. Thekackra, “The Solar Cell Constant and Solar Spectrum Measurement from a Research Aircraft,” NASA Technical Report, (1970)
13. D. A. Neamen, “Semiconductor Physics and Devices,” (2003)
14. http://en.wikipedia.org/wiki/PECVD
15. http://en.wikipedia.org/wiki/Scanning_electron_microscope
16. http://en.wikipedia.org/wiki/Transmission_electron_microscopy

17. Keith Emery, “Measurement and Characterization of Solar Cells and Modules,” in *Handbook of Photovoltaic Science and Engineering*, John Wiley & Sons, New York, 701-752, (2003).
18. D. J. Aiken, ”High performance anti-reflection coatings for broadband multi-junction solar cells”, Sol. Energy Mater. Sol. Cells **64**, 393, (2000).
19. W. H. Southwell, “Gradient-index antireflection coatings”, Opt. Lett. **8**, 584-586, (1983).
20. J. A. Dobrowolski, D. Poitras, P. Ma, H. Vakil, M. Acree, “Toward perfect antireflection coatings: numerical investigation”, Appl. Opt. **41**, 3075-3083. (2002).
21. D. Poitras, J. A. Dobrowolski, “Toward perfect antireflection coatings. 2. Theory, ”Appl. Opt. **43**, 1286, (2004).
22. 趙建昌, “Optics and Electronics Simulation of Surface Plasmon Enhanced Silicon Thin Film Solar Cells,” Ph. D. Thesis, NCU, Taiwan, R.O.C. (2010)
23. J. J. Hench and Z. Strakos, “The RCWA method – a case study with open questions and perspectives of algebraic computations,” Electron. Trans. Num. Anal. 31, 331-357 (2008).
24. J. M. Nunzi, “Organic photovoltaic materials and devices,” *Comptes Rendus Physique* **3**, 2002, pp. 523-542.
25. P. Lalanne and G. M. Morris, “Design, fabrication and characterization of subwavelength periodic structures for semiconductor anti-reflection coating in the visible domain,” *Proc. SPIE* **2776**, 1996, pp. 300-309.
26. D. J. Aiken, “Hight performance anti-reflection coatings for broadband multi-junction solar cells,” *Sol. Energy Mater. Sol. Cells* **64**, 2000, pp. 393.
27. L. Zeng, P. Bermel, Y. Yi, B. A. Alamariu, K. A. Broderick, J. Liu, C. Hong, X. Duan, J. Joannopoulos and L. C. Kimerling, “Demostration of enhanced absorption in thin film Si solar cells with textured photonic crystal back reflector,” *Appl. Phys. Lett.* **93**, 2008, 221105.

28. P. Bermel, C. Luo, L. Zeng, L. C. Kimerling and J. D. Joannopoulos, “Improving thin-film crystalline silicon solar cell efficiencies with photonic crystals,” *Opt. Express* **15**, 2007, pp. 16986-17000.

29. N. N. Feng, J. Michel, L. Zeng, J. Liu, C. Y. Hong, L. C. Kimerling and X. Duan, “Design of highly efficient light trapping structures for thin-film crystalline silicon solar cells,” *IEEE T. Electron Dev.* **54**, 2007, pp. 1926-1933.

30. M. Y. Chiu, C. H. Chang, M. A. Tsai, F. Y. Chang, and Peichen Yu, “Improved optical transmission and current matching of a triple-junction solar cell utilizing sub-wavelength structures,” Opt. Express **18**, A308-A313 (2010).

31. M. A. Tsai, P. Yu, C. H. Chiu, H. C. Kuo, T.C. Lu, and S. H. Lin, ”Self-Assembled two-dimensional surface structures for beam shaping of GaN-based vertical-injection light-emitting diodes,” IEEE Photonics Technol. Lett. **22**, 12-14 (2010).

32. C. H. Chiu, P. Yu, H. C. Kuo, C. C. Chen, T.C. Lu, S. C. Wang, S. S. Hsu, Y. J. Cheng and Y. C. Chang, “Broadband and omnidirectional antireflection employing disordered GaN nanopillars,” Opt. Express **16**, 8748-8753 (2008) .

33. M. A. Tsai, P. C. Tseng, H. C. Chen, H. C. Kuo, and P. Yu, “Enhanced conversion efficiency of a crystalline silicon solar cell with frustum nanorod arrays,” Opt. Express **19**, A28-A34 (2011) .

34. Y. Kanamori, M. Sasaki, and K. Hane, “Broadband antireflection gratings fabricated upon silicon substrates,” Opt. Lett., **24**, 1422-1424 (1999).

35. S. Y. Chou, P. R. Krauss, P. J. Renstrom, “Imprint of sub-25 nm vias and trenches in polymers,” Appl. Phys. Lett., **67**, 3114-3116, (1995).

36. M. D. Austin, H. Ge, W. Wu, M. Li, Z. Yu, D. Wasserman, S. A. Lyon, Stephen Y. Chou, “Fabrication of 5 nm linewidth and 14 nm pitch features by nanoimprint lithography,” Appl. Phys. Lett., **84**, 5299-5301, (2004).

37. K. Ansari, J. A. van Kan, A. A. Bettiol, and F. Watt , “Fabrication of high aspect ratio 100 nm metallic stamps for nanoimprint lithography using proton beam writing,” Appl. Phys. Lett., **85**, 476-478, (2004).

38. Boden, S.A., Bagnall, D.M., “Bio-mimetic subwavelength surface for near-zero reflection sunrise to sunset,”2006, In: Proceedings of the Fourth World Conference on Photovoltaic Energy Conversion, Hawaii.

39. Y. Kanamori, E. Roy, Y. Chen, “Antireflection sub-wavelength gratings fabricated by spin-coating replication,” Microelectron. Eng. **78**, 287-293, (2005).

40. Shemaiah M. Weekes, Feodor Y. Ogrin, William A. Murray, and Paul S. Keatley, “Macroscopic arrays of magnetic nanostructures from self-assembled nanosphere templates,” Langmuir**, 23**, 1057-1060, (2007).

41. D. F. Liu, Y. J. Xiang, X. C. Wu, Z. X. Zhang, L. F. Liu, L. Song, X. W. Zhao, S. D. Luo, W. J. Ma, J. Shen, W. Y. Zhou, G. Wang, C. Y. Wang, and S. S. Xie, “Periodic ZnO nanorod arrays defined by Polystyrene microsphere self-assembled monolayers,” Nano. Lett. **6**, 2375-2378, (2006).

42. Y. J. Zhang, “Application of two-dimensional polystyrene arrays in the fabrication of the ordered silicon pillars,” Journal of Alloys and Compounds, **450**, 512-516 (2008).

43. P. Jiang, T. Prasad, M. J. McFarland, and V. L. Colvin, “ Two-dimensional nonclose-packed colloidal crystals formed by spincoating,” Appl. Phys. Lett.,**89**, 011908, (2006).

44. P. Jiang, M. J. McFarland, “Large-scale fabrication of wafer-size colloidal crystals macroporous polymers and nanocomposites by spin-coating,” J. Am. Chem. Soc., **126**, 13778, (2004).

45. C.H. Sun, P. Jiang, B. Jiang, “Broadband moth-eye antireflection coating on silicon,” Appl. Phys. Lett., **92**, 061112, (2008).

46. Bailey R C, Stevenson K J and Hupp J T, “Assembly of Micropatterned Colloidal Gold Thin Films via Microtransfer Molding andElectrophoretic Deposition,” Adv. Mater.,**12,**1930, (2000).

47. Z.Z. Gu, Akira Fujishima and Osamu Sato, “Fabrication of High-Quality Opal Films with Controllable Thickness,” Chem. Mat., **14**, 760-765, (2002).

48. C.-M. Hsu, S. T. Connor, M. X. Tang, and Yi Cui, “Wafer-scale silicon nanopillars and nanocones by Langmuir–Blodgett assembly and etching,” Appl. Phys. Lett., 93, 133109, (2008).

49. J. Zhu, Z. Yu, G. F. Burkhard, C.-M. Hsu, S. T. Connor, Y.Xu, Qi Wang, M. McGehee, S. Fan, Yi Cui, “Optical absorption enhancement in amorphous silicon nanowire and nanocone arrays,” Nano Lett., in published, (2010).

50. W. H. Southwell, “Gradient-index antireflection coatings”, Opt. Lett. **8**, 584-586, (1983).

51. J. A. Dobrowolski, D. Poitras, P. Ma, H. Vakil, M. Acree, “Toward perfect antireflection coatings: numerical investigation”, Appl. Opt. **41**, 3075-3083. (2002).

52. D. Poitras, J. A. Dobrowolski, “Toward perfect antireflection coatings. 2. Theory, ”Appl. Opt. **43**, 1286, (2004).

53. P. Lalanne, G. M. Morris, “Antireflection behavior of silicon subwavelength periodic structures for visible light”, Nanotechnology, **8**, 53, (1997).

54. D. S. Hobbs, R. D. Macleod, J. R. Riccobono, “Update on the development of surface relief micro-structures”, Proc. of SPIE, **6545**, 65450Y, (2007).

55. Bernhard, C. G. & Miller, W. H., “ A corneal nipple pattern in insect compound eyes,” Acta Physiol. Scand. **56**, 385–386, (1962).

56. D. G. Stavenga, S. Foletti1, G. Palasantzas and K. Arikawa, “Light on the moth-eye corneal nipple array of the butterflies,” Proceedings of the Royal Society B, **273**, 661-667, (2006).

57. W. Ley, E. Plescher, A. Freiburg, N. Nikolaizig, and A. Popvitch, “SUN Simulator Calibration Procedure,” Environmental Testing for Space Programms, 1997, pp.339-344.